Modeling tabular icebergs submerged in the ocean

A. A. Stern[1] , **A. Adcroft**[1] , **O. Sergienko**[1] , **G. Marques**[1]

[1]Geophysical Fluid Dynamics Laboratory, Princeton University
[1]201 Forrestal Rd, Princeton, NJ 08540, USA

Key Points:

- A novel modeling framework is developed to explicitly model large tabular icebergs submerged in the ocean.
- Tabular icebergs are represented using Lagrangian elements that drift in the ocean, and are held together by numerical bonds.
- Breaking the numerical bonds allows us to model iceberg breakup and calving.

Corresponding author: Alon Stern, `sternalon@gmail.com`

Abstract

Large tabular icebergs calved from Antarctic ice shelves have long lifetimes (due to their large size), during which they drift across large distances, altering ambient ocean circulation, bottom-water formation, sea-ice formation, and biological primary productivity in the icebergs' vicinity. However, despite their importance, the current generation of ocean circulation models usually do not represent large tabular icebergs. In this study we develop a novel framework to model large tabular icebergs submerged in the ocean. In this framework, tabular icebergs are represented by pressure-exerting Lagrangian elements that drift in the ocean. The elements are held together and interact with each other via bonds. A breaking of these bonds allows the model to emulate calving events (i.e. detachment of a tabular iceberg from an ice shelf) and tabular icebergs breaking up into smaller pieces. Idealized simulations of a calving tabular iceberg, its drift, and its breakup demonstrate capabilities of the developed framework.

1 Introduction

Large tabular icebergs – pieces of floating ice with horizontal dimensions substantially larger than the vertical dimension – calve infrequently ($\sim$ every forty-fifty years) from Antarctic or Greenlandic ice shelves [Jacobs et al, 1992]. Observational estimates suggest that over the past 30 years approximately half of Antarctic ice-shelf decay is due to iceberg calving, while the other half occurs through ice-shelf melting [Depoorter et al, 2013; Rignot et al, 2013]. The infrequently-calved tabular icebergs (horizontal extent larger than 5 km) account for more than 90% of the Southern Hemisphere iceberg mass [Tournadre et al, 2016].

After calving, icebergs drift away from their origins, often becoming stuck in sea ice, or grounding on bathymetric highs along the Antarctic coast [Lichey and Hellmer, 2001; Dowdeswell and Bamber, 2007]. Large tabular icebergs extend deep into the water column, and have the potential to disrupt ocean circulation patterns for months or even years after calving [Robinson et al, 2012; Stern et al, 2015]. The freshwater flux from iceberg melt impacts ocean hydrography around the iceberg, influencing sea-ice production and bottom-water formation [Arrigo et al, 2002; Robinson et al, 2012; Nicholls et al, 2009; Fogwill et al, 2016]. Because of their large size, the tabular icebergs have long lifetimes during which they drift over long distances injecting meltwater along the way and impacting the Southern Ocean state (e.g. hydrography, sea-ice conditions, etc.) far away from their calving origins [Stern et al, 2016; Rackow et al, 2017]. Meltwater injection (and the accompanying upwelling) from icebergs can also influence biological productivity by bringing nutrients to the surface ocean or changing sea-ice conditions [Arrigo et al, 2002; Vernet et al, 2012; Biddle et al, 2015]. The increased productivity associated with free-floating tabular icebergs has been linked with local increases in ocean carbon uptake, potentially large enough to be a significant fraction of the Southern Ocean carbon sequestration [Smith et al, 2007].

In recent years, there has been an increased interest in iceberg drift and decay. This surge of interest has been driven by (i) the need to understand polar freshwater cycles in order to create realistic climate change and sea level projections [Silva et al, 2006; Shepherd and Wingham, 2007; Rignot et al, 2013]; and (ii) the increased navigation and exploration activities in high-latitude iceberg-filled waters in the Arctic [Pizzolato et al, 2012; Unger, 2014; Henderson and Loe, 2016]. The increased interest in icebergs has led to the development of numerical models of iceberg drift and decay [Mountain, 1980; Bigg et al, 1997; Gladstone et al, 2001; Kubat et al, 2005], some of which have been included in global General Circulation Models [Martin and Adcroft, 2010; Marsh et al, 2015]. These iceberg drift models treat icebergs as levitating Lagrangian point particles, which are advected by the flow, and melt according to parameterizations for iceberg melt. Here the term *levitating* refers to the fact the point-particle icebergs do not apply pressure to the

ocean surface, and therefore do not displace water. Since icebergs are treated as point particles, iceberg drift models are mostly suitable for modeling icebergs smaller than an ocean grid cell. Consequently, these models have mostly been used to represent icebergs smaller than 3.5 km on a global scale [Jongma et al, 2009; Martin and Adcroft, 2010; Marsh et al, 2015].

Point-particle iceberg drift models are less suitable for modeling larger tabular icebergs, where the size and structure of the iceberg may be an important feature in determining their drift and decay [Stern et al, 2016]. They also are not suitable for studying the local effects that icebergs have on the surrounding ocean, or the small-scale processes that influence iceberg melt and decay [Wagner et al, 2014; Stern et al, 2015]. For these reasons, tabular icebergs are currently not represented in the iceberg drift models used as components of climate models, despite accounting for the vast majority of the total Southern Hemisphere iceberg mass [Tournadre et al, 2016].

Some efforts have been made to modify levitating point-particle icebergs models so that they can be used to represent tabular icebergs [Lichey and Hellmer, 2001; Hunke, 2011; Rackow et al, 2017]. A promising approach involves integrating ocean properties over the implied iceberg surface area [Rackow et al, 2017] or implied iceberg depth [Hunke, 2011; Merino et al, 2016] when calculating the iceberg forcing (or applying iceberg melt fluxes), to account for the horizontal and vertical extent of the tabular iceberg. However, this approach does not account for influence that a submerged iceberg can have on the surrounding ocean due to its physical presence in the water column. Martin and Adcroft [2010] partially addressed this by allowing their icebergs to apply pressure to the top-most layer of their layered ocean model. This approach effectively allowed the icebergs to displace water, therefore making the point-particle icebergs into 'non-levitating' (pressure-exerting) icebergs. A limitation of the Martin and Adcroft [2010] approach is that the maximum iceberg size is constrained to be smaller than one ocean grid cell, which means that tabular icebergs can not be represented [Stern et al, 2016]. While it may be possible to combine these two approaches, at this stage more work is needed before point-particle icebergs can be used to represent tabular icebergs in climate models. Furthermore, at smaller scales and for regional modeling, it is clear that modeling tabular icebergs as levitating point particle is not adequate to resolve the complex interactions between tabular icebergs and the surrounding ocean.

The goal of this study is to develop a new framework to model all kinds of icebergs, where tabular icebergs are explicitly resolved in the ocean. Our new representation of icebergs aims to include the following key properties: (i) icebergs should be able to travel large distances within the ocean, (ii) icebergs should melt and decay as they drift in the ocean, (iii) icebergs should behave as if they have finite extent and should be able to have any shape and size, (iv) icebergs should be submerged in the ocean so they are no longer levitating, and (v) tabular icebergs should be able to break away from ice shelves or break into smaller pieces. Properties (i) and (ii) are common to point-particle icebergs models, while properties (iii), (iv) and (v) are new to the framework developed in this study. A further requirement of the new framework is that the model should run sufficiently fast to be included in general circulation models used for climate.

In order to allow icebergs to travel large distances, we model the icebergs in a Lagrangian framework (as in the point particle iceberg drift models described above). However, in our model icebergs are no longer treated as point particles that interact with the ocean at a single location. Instead icebergs are given physical structure, so that they interact with the ocean across multiple ocean grid cells, depress the ocean surface over a wide area, and can interact with other icebergs (Figure 1). This is done by assigning a finite surface area and shape to the Lagrangian elements, which allows the elements to behave as if they have a finite extent. The finite extent of an element is transmitted by the ocean by distributing the element's weight, surface area and melt fluxes over multiple ocean grid cells in a way which is consistent with the shape of the ice element. Finite-

extent elements interact with each other via repulsive forces which are applied when the boundaries of the elements overlap. This prevents the icebergs from piling up on top of one another, which has been an issue near coastlines in previous point-particle icebergs models.

Large tabular icebergs can then be represented by 'bonding' together multiple ice elements into larger structures using numerical bonds (Figure 1). The numerical bonds hold the ice elements together and allow a collection of elements to move as a unit. This allows tabular icebergs to drift in the ocean when forced by ocean currents and wind. An advantage of representing tabular icebergs using numerical bonds is that by breaking the bonds, we can simulate iceberg calving (e.g.: Figure 2), or the response to an iceberg fracturing into multiple smaller pieces (see movies S1 and S2 in the Supporting Information).

The manuscript is organized as follows. Section 2 gives a description of the key aspects of the model developed in this study. Since this model is a new approach to modeling icebergs, we present technical aspects of the model. In Sections 3 and 4, we demonstrate the capabilities of the model by simulating a tabular iceberg detaching from an idealized ice shelf. In a further simulation we break some numerical bonds within the tabular iceberg to demonstrate an iceberg splitting in two.

2 Model description

The Kinematic Iceberg Dynamics model (KID) is a Lagrangian particle-based model in that the objects of the model are Lagrangian elements [Cundall and Strack, 1979; Luding, 2008; Radjai and Dubois, 2017]. Each element represents a column of ice that is floating in the ocean, and has a position, velocity, mass, and a set of dimensions, which can evolve in time. The motion of each element is determined by a momentum equation which is solved in the (Lagrangian) reference frame of the element. The elements experience oceanic and atmospheric forces, which are either prescribed, or computed by coupling the iceberg model to an ocean/atmosphere model. The ice elements also interact with one another via attractive and repulsive interactive forces, and can be bonded together to form larger structures. The angular momentum of the elements is not modeled explicitly; instead rotational motion of larger structures emerge as a consequence of bond orientation and collective motion.

In different contexts, the ice elements can be thought to represent individual icebergs, sea-ice flows, or, when the elements are bonded together, they can represent larger structures such as tabular icebergs or ice shelves.

The KID model is developed on the code base of an existing iceberg drift model [Martin and Adcroft, 2010; Stern et al, 2016]. When run with a different set of runtime flags, the model runs as a traditional point-particle iceberg drift model.

2.1 Equations of motion

The elements drift in the ocean in response to atmosphere, ocean and sea-ice drag forces, as well as the Coriolis force, a wave radiation force, a force due to the sea surface slope and interactive forces with other elements. The momentum equation for each element is given by

$$M\frac{D\vec{u}}{Dt} = \vec{F}_A + \vec{F}_W + \vec{F}_R + \vec{F}_C + \vec{F}_{SS} + \vec{F}_{SI} + \vec{F}_{IA}, \tag{1}$$

where $\frac{D}{Dt}$ is the total (Lagrangian) derivative, M is the mass of the element, $\vec{u}$ is the velocity of the element, and the terms on the right hand side give the forces on the element due to air drag ($\vec{F}_A$), water drag ($\vec{F}_W$), sea-ice drag ($\vec{F}_{SI}$), Coriolis force ($\vec{F}_C$), wave radiation force ($\vec{F}_R$), sea surface slope ($\vec{F}_{SS}$), and interactions with other elements ($\vec{F}_{IA}$).

When ice elements move alone (without interactions with other elements), they can be thought of as representing individual (or clusters of) small icebergs, and follow the same equations described in the iceberg drift model of Martin and Adcroft [2010] (based on the equations outlined in Bigg et al [1997] and Gladstone et al [2001]). A description of these forces is provided in Appendix A.

In addition to the external forces, the ice elements experience interactive forces due to the presence of other elements. Two types of interactive forces are included between elements. The first force is a repulsive force which is applied to elements to prevent them from overlapping the boundaries of the neighboring elements. The second interactive force is a force due to numerical 'bonds', and is only applied if two elements are labelled as 'bonded'. When two elements are bonded, each element feels an attractive force that prevents the elements from moving too far apart from one another. The details of the interactive forces are provided in below.

2.2 Interactive Forces

The interactive forces in the model are used to (i) prevent the ice elements from overlapping and (ii) to connect multiple ice elements together so that the collection of elements moves as a rigid body. Modeling the collisions and movements of rigid objects precisely, requires very small time steps and precise collision detection algorithms, which are very computationally expensive. Models using these methods are typically only run for a few days or even a few seconds, and are used to study rapid processes like crack formation or ridging [Hopkins, 2004; Bassis and Jacobs, 2013; Rabatel et al, 2015]). The tabular iceberg framework presented in this study is developed in order to be used in general circulation models used for multi-year simulations. In order to gain the required computational efficiency, we relax the requirement that icebergs must be perfectly rigid and that ice elements can not overlap. Instead, we model the interactive forces between ice elements using damped elastic forces, which can be calculated more efficiently.

The total interactive force on an element is calculated by adding together the interactions with all other elements, such that the interactive force on element i, $(\vec{F}_{IA})_i$ is given by:

$$(\vec{F}_{IA})_i = \Sigma_{j \neq i}(\vec{F}_{IA})_{ij}, \tag{2}$$

where $(\vec{F}_{IA})_{ij}$ is the force on element i by element j. Both bonded and repulsive interactions are modeled using elastic stresses with frictional damping. The elastic component of the force is a function of the distance between the two elements, while the frictional damping force depends on the relative velocity of the two elements.

To describe the forces between two elements, we begin by introducing some notation. Let $\vec{x_i}$, $\vec{x_j}$ be the positions of elements i and j. The distance between elements i and j is

$$d_{ij} = |\vec{x_i} - \vec{x_j}|. \tag{3}$$

In calculations of the interactive forces between elements, the elements are assumed to be circular. We define the interaction radius of an element by

$$R_i = \sqrt{\frac{A_i}{\pi}}, \tag{4}$$

where A_i is the planar surface area of element i. Using this, we define the critical-interactive-length scale,

$$L_{ij} = R_i + R_j, \tag{5}$$

which governs interactions between elements i and j. Repulsive forces are only applied when $d_{ij} < L_{ij}$, while for $d_{ij} > L_{ij}$ attractive bonded forces are applied when a bond exists between element i and j (see diagram in Figure 3). The interactive forces are designed such that (in the absence of other external forces) bonded particles will settle in an equilibrium position where elements are separated by L_{ij}.

To aid in notation, we define a bond matrix B_{ij} such that $B_{ij} = 1$ if elements i and j are bonded together and $B_{ij} = 0$ otherwise. Using this notation, the interactive force $(\vec{F}_{IA})_{ij}$ on an element i by an element j is given by

$$(\vec{F}_{IA})_{ij} = \begin{cases} (\vec{F}_e)_{ij} + (\vec{F}_d)_{ij} & \text{if } (d_{ij} \leq L_{ij}) \text{ or } (d_{ij} > L_{ij} \text{ and } B_{ij} = 1) \\ 0 & \text{if } d_{ij} > L_{ij} \text{ and } B_{ij} = 0 . \end{cases} \quad (6)$$

$(\vec{F}_e)_{ij}$ and $(\vec{F}_d)_{ij}$ are the elastic and frictional damping components of the interactive force between elements i and j. The elastic force $(\vec{F}_e)_{ij}$ between elements is given by

$$(\vec{F}_e)_{ij} = -\kappa_e \left(d_{ij} - L_{ij} \right) M_{ij} \vec{r}_{ij}, \quad (7)$$

where $\vec{r}_{ij} = \frac{(\vec{x_i} - \vec{x_j})}{|\vec{x_i} - \vec{x_j}|}$ is the directional unit vector between the position of element i and j, κ_e is the spring constant, and M_{ij} is the minimum of the masses of elements i and j. The interactive forces obey Newton's 3rd Law (i.e.: $(\vec{F}_{IA})_{ij} = -(\vec{F}_{IA})_{ji}$). The minimum mass, M_{ij}, is preferred to the average mass, since this means that for two bonded elements a fixed distance apart, the acceleration due to elastic forces is bounded, even when the mass of one of the elements approaches zero.

The frictional damping force acts to dampen the relative motion of the two particles. If $P_{\vec{r}_{ij}}$ is the projection matrix that projects onto $\vec{r}_{ij}$, then the frictional damping force is given by

$$(\vec{F}_d)_{ij} = -M_{ij} c_{r_{||}} P_{\vec{r}_{ij}} \cdot (\vec{u_i} - \vec{u_j}) \quad (8)$$

Here $c_{r_{||}}$ is the drag coefficient damping motion parallel to $\vec{r}_{ij}$. We set $c_{r_{||}} = 2\sqrt{\kappa_e}$, so that the elastic force parallel to $\vec{r}_{ij}$ is critically damped. The damping force is implemented using an implicit time stepping scheme, to avoid stability issues for very small elements (details found in Appendix B).

Figure 4 illustrates the effectiveness of the repulsive forces in an uncoupled (ice-only) simulation. In this simulation ice elements are forced westward into a bay, and eventually come to rest in the bay with a small amount of overlap between elements. The amount of overlap between elements in the final state of the simulation depends on the magnitude of the spring constant, κ_e, with larger spring constants reducing the amount of overlap. Increasing the spring constant also makes the system numerically stiff so that smaller time steps are required to prevent numerical instabilities (the system is stable for time steps satisfying $dt^2 < 4/\kappa_e$). A value of $\kappa_e = 10^{-5}$ s^{-2} is chosen that is large enough to prevent too much overlap between elements for typical ocean forcings (e.g: Figure 4), and small enough to allow for time steps up to 10 minutes (smaller time steps are used when the model is coupled to an ocean model).

Figure 5 illustrates the effectiveness of the numerical bonds in simulations of small icebergs (individual un-bonded elements) and large icebergs (constructed from many ice elements bonded together) forced to drift towards a convex coast line. When the tabular icebergs arrive at the coast, they bump into the coastline and begin to rotate, influencing the paths of the other icebergs. This example illustrates an advantage of using small elements bonded together to represent large-scale structure - i.e. rotational motion of large structures can be simulated without explicitly accounting for the angular momentum of the elements (as discussed in Jakobsen [2001]). Movies of these uncoupled simulations are found in S3 and S4 in the Supporting Information.

2.3 Initializing element geometry and packing

For purposes of initialization, we assume that elements have surface areas which are shaped as equally-sized regular hexagons (note that the elements are assumed to be circular for propose of interactions). When packing elements together, the hexagonal elements are initially arranged in a staggered lattice, with each element bonded to the adjacent elements (Figures 1 and 6a). In this arrangement, each element (away from the

edges) is bonded to six other elements. The bonds between elements form a pattern of equilateral triangles, which gives rigidity to the larger structure. The circular shape of elements (used for interactions) is inscribed within the hexagonal shape used for packing (Figure 6a). The centers of adjacent elements are initially separated by a distance $d_{ij} = L_{ij} = 2A_p$, where A_p is the length of the apothems of the hexagons.

Some experiments were also performed using rectangular elements, arranged in a regular (non-staggered) lattice. In this case, each element forms four bonds with adjacent elements. However, the resultant structures were found to be much less rigid and tended to collapse when sufficient forces were applied. For this reason, we only show the results using hexagonal elements.

2.4 Ice-ocean coupling

The KID model is coupled to the ocean model via a two-way synchronous coupling, meaning that ocean-model fields are passed to the iceberg model, and iceberg model fields are passed back to the ocean model at every time step. Passing fields between the two models involves interpolating the fields from the ocean model's Eulerian grid onto the iceberg model's 'Lagrangian grid' (i.e.: onto the ice elements), and aggregating fields from the Lagrangian elements onto the ocean-model's Eulerian grid.

The coupling from the ocean model to the iceberg model is straight forward: at every time step the top-of-ocean temperature, salinity, velocity and sea-ice concentration are passed from the ocean model to the iceberg model, to be used in the momentum and thermodynamic equations of the ice elements. Since tabular icebergs are explicitly resolved in the ocean, it is sufficient for each element to interact with only the upper-most ocean layer. This layer could be hundreds of meters below mean-global sea level if a large iceberg was positioned above it. This means that there is no need to manually embed icebergs into the ocean by integrating ocean fields over the icebergs' thickness, as suggested in Merino et al [2016], or to integrate ocean fields over an implied iceberg surface area, as suggested in Rackow et al [2017]. Within the iceberg model, the ocean model fields are interpolated onto the Lagrangian grid using a bilinear interpolation scheme.

The iceberg model influences the ocean by: (i) applying a pressure to the ocean surface, (ii) affecting the upper ocean by applying a no-slip boundary condition and frictional velocity beneath the ice, and (iii) imposing heat, salt and mass fluxes on the ocean, associated with ice melting. Six fields are passed from the iceberg model to the ocean model: ice mass, ice area, frictional velocity, and heat, salt and mass fluxes. Fields in the iceberg model are aggregated from the Lagrangian elements to the Eulerian ocean grid before they are passed to the ocean model.

The aggregation of the iceberg-model fields onto the ocean grid is done in a way that is consistent with the shape of the elements in the iceberg model (see Section 2.3). Fields are 'spread' to the ocean model grid by exactly calculating what fraction of an element's surface area lies in a particular grid box, and dividing the field in proportion to this fraction. As an example, consider a hexagonal element in the iceberg model, which is positioned such that it intersects four ocean grid cells (Figure 6b). In this situation, the element's mass (for example) is divided between these four ocean cells in proportion to the overlap area between the hexagonal element and the grid cell (this fraction is shown by the colors in Figure 6b). An advantage of this approach is that there are no jumps in pressure as an element moves from one grid cell to another, which could trigger artificial tsunamis within the ocean model.

The numerical calculation of the intersection between hexagons and the ocean grid is simplified by dividing the hexagon into 6 equilateral triangles. This method allows for the intersection to be found even when the hexagon is not aligned with the grid.

The aggregation scheme is coded with the restriction that an element's area can only intersect a maximum of four ocean grid cells at a time. A consequence of this is that this sets a limit on the maximum size of elements that can be represented using this model, i.e., the longest horizontal dimension of an ice element must be smaller than the ocean grid spacing. Larger ice structures are constructed by bonding together smaller elements.

2.5 Melting parameterization

The ice elements change their mass and size due to melting, which also affects the surrounding ocean by changing its heat and salt content. In the model, these processes are parametrized in several ways. In this section we describe the melt parametrization for bonded, unbonded and partially bonded elements.

As mentioned above, ice elements which do not interact with other elements are modeled identically to the point particle icebergs described in Martin and Adcroft [2010]. These elements melt according to three semi-empirical parametrization for melt commonly used in previous iceberg studies [Gladstone et al, 2001; Martin and Adcroft, 2010]. Three types of iceberg melting are distinguished: basal melt, M_b, melt due to wave erosion, M_e and melt due to buoyant convection, M_v. The melt rates M_e and M_v are applied to the sides of the ice element, while M_b is applied at the ice element base. The details of M_b. M_v and M_e are given in Appendix A.

When multiple elements are bonded together to form larger structures, it is no longer appropriate to use the melt parameterizations developed for individual point-particle icebergs. An element which is completely surrounded by other elements, is meant to represent a column of ice in the middle of a large structure, and hence will not experience melt at its sides due to wave erosion or buoyant convection. Also, the iceberg basal melt rate M_b described above is based on boundary layer theory of flow past a finite plate, and is only appropriate for basal surfaces where the distance from the leading edge is sufficiently small [Eckert, 1950; Weeks and Campbell, 1973]. For an element in the interior of a large structure, the distance from the edge of the structure is large, and so using M_b for the basal melt is not appropriate. Instead, the basal melt M_s is determined using the three equation model for basal melt, which is a typical melting parametrization used beneath ice shelves [Holland and Jenkins, 1999], and has been used to parametrize melt rates beneath large icebergs in previous studies [Silva et al, 2006; Rackow et al, 2017].

When using both individual elements and bonded elements in the same simulation, we determine which melt rate parameterizations to use based on the amount of bonds that each element has. An element in the center of a large structure has the maximum number of bonds, while an un-bonded element has no bonds. If an element can have maximum number of bonds $N_{\max}$, and the number bonds that an element has is N_b, then the fraction of the element's perimeter surrounded by ocean (rather than by other ice elements) is estimated as $\epsilon = 1 - \frac{N_b}{N_{\max}}$. In this case, the element experiences side melt and bottom melt

$$M_{\text{side}} = \epsilon(M_v + M_e) \tag{9}$$

and

$$M_{\text{bottom}} = \epsilon M_b + (1 - \epsilon)M_s, \tag{10}$$

respectively. In this way, elements with no bonds (i.e.: $\epsilon = 1$), melt like point-particle icebergs; elements at the center of large structures (i.e.: $\epsilon = 0$) melt like ice shelves; and elements at the sides of large structures have a combination of iceberg side and basal melt, and ice-shelf melt.

A similar procedure is used to allow elements at the edge of a large structure to experience partial side drag and wave radiation forces, while for interior elements the side drag force is zero. Details are provided in Appendix A.

2.6 Algorithms and computational efficiency

Including interactions between elements leads to an increase in the computational complexity of the model. In this subsection we comment on some of the algorithmic procedures that have been used to increase the computational efficiency.

2.6.1 Interactions and Bonds

At every time step, we calculate the force on each element due to interactions with every other element. This involves order N^2 operations (for N elements), which becomes computationally expensive as N grows large. We reduce the number of computations using a space-partitioning contact search where we leverage the fact that each element only has repulsive interactions with elements that are less than one ocean grid cell away, and each element only has bonded interactions with a small number of other elements.

The computation reduction is achieved by storing the element data in an efficient way that eliminates a search through all element pairs to check if they are close to one another or are bonded with one another. The data storage system is organized as follows: pointers to the memory structures containing each element are stored in linked list data structures, which allow elements to be added and removed from the lists easily without restructuring the entire list. Instead of using one list for all the elements on a processor (as was done in the original code [Martin and Adcroft, 2010]), we use a separate linked list for each ocean grid cell. When an element moves between ocean grid cells, it is removed from its original list and added to the list corresponding to its new ocean grid cell. Since the area of elements has to be smaller than the area of an ocean grid cell, the critical interaction length scale (equation 5) is less than the size of a grid cell. This means that elements only experience repulsive forces with other elements in the same ocean grid cell, or in one of the 8 adjacent cells. At each time step and for each element i, the code traverses the linked lists of the 9 surrounding grid cells, and applies a repulsive force if $d_{ij} < L_{ij}$ (whether the elements are bonded or not). Limiting the possible repulsive interactions to elements in these 9 linked lists substantially reduces the computational time needed to calculate the total interactive forces.

The attractive forces are computed in the following way. Each bond is assigned two pieces of memory (one for each of the two elements involved in the bond). Each ice element contains a linked list of each of its bonds (typically up to six bonds per element). At every time step, the code traverses the lists of bonded elements, and adds an attractive bonded force corresponding to these bonds if $d_{ij} > L_{ij}$ (the repulsive bonded force to be applied when $d_{ij} < L_{ij}$ is already accounted for by the procedure outlined in the previous paragraph). Having a list of bonds stored with each element reduces the computations needed for bonded interactions from order N^2 to order N. Computing attractive forces separately from the repulsive forces allows us to avoid checking whether two elements are bonded, which further increases the computational efficiency.

2.6.2 Parallelization and halos

The iceberg model runs on multiple processors in parallel (using the same grid decomposition as the ocean model). When elements move from an ocean cell on one processor to an ocean cell on a second processor, the memory has to be passed from one processor to the next, added to and removed from the appropriate lists, and the memory has to be allocated and deallocated correctly. Element interactions across the edge of processors are handled using computational halos. A computational halo is a copy of the edge of one processor which is appended to the edge of a second processor, so that the first processor can interact with the second processor during a time step. Before each time step, elements at the edges of each processor are copied onto the halos of adjacent processors so that they can be used in calculating the interactive forces. After each time

step, these halos are emptied, and the process is repeated. These halo updates are one of the most computationally expensive parts of the iceberg model. Details of how the bonds are broken and reconnected across processor boundaries are provided in Appendix C.

2.6.3 Time stepping

The elements in the iceberg model are advected using a semi-implicit velocity Verlet time-stepping scheme. The velocity Verlet time stepping scheme is commonly used in discrete element models in video games because it is computational efficient and has desirable stability properties [Jakobsen, 2001]. This time stepping scheme was preferred to the Runge-Kutta 4, which was used in the iceberg model of Martin and Adcroft [2010] since the Verlet time stepping only requires one calculation of the interactive forces once per time step (while the Runge-Kutta scheme requires the interactive forces to be calculated four times). Since the calculation of the interactive forces is one of the most computationally expensive part of the algorithm, the Verlet scheme leads to a significant increase in the computational efficiency of the model. The Verlet scheme used in the model contains a modification of the original (fully explicit) velocity Verlet time stepping scheme in that damping terms are treated implicitly (which increases the numerical stability). The details of this adapted time stepping schemed are outlined in Appendix B.

3 Experiment Setup

The introduction of Lagrangian elements, numerical bonds and interpolation schemes between the Eulerian and Lagrangian grids (discussed in Section 2) means that we now have the tools to model large tabular icebergs submerged in the ocean. We demonstrate this capability by simulating a tabular iceberg drifting away from an ice shelf in an idealized setting.

3.1 Model configuration

We use the geometric setup of the Marine Ice Ocean Modeling Inter-comparison Project (MISOMIP) [Asay-Davis et al, 2016]. The configuration consists of an idealized ice shelf in a rectangular domain. The domain is $L_x = 80$ km wide and $L_y = 480$ km long, and contains an ice shelf which is grounded on the south side of the domain and has an ice front at y=650 km. The ice thickness and bottom topography of this setup are shown in Figure 7a and 7c respectively, with the grounding line position drawn in for reference. The configuration is the same as that of the Ocean0 setup in the MISOMIP, with a few minor changes to the ice-shelf geometry (see the Supporting Information for details).

3.2 Initializing Lagrangian elements

The idealized ice shelf is constructed out of Lagrangian ice elements. Ice elements are hexagonal and are arranged in a regular staggered lattice (as discussed in Section 2.3). The sides of the hexagons are initialized with length $S = 0.98$ km. Gaps along the boundaries of the domain are filled in using smaller elements so that the total ice-shelf area is preserved. These smaller elements are held stationary throughout the simulations, and are not bonded to other elements.

The initial masses of the ice elements are calculated from the gridded ice thickness field using bilinear interpolation, assuming a constant ice density $\rho = 918$ kg/m^3. When the model runs, the mass of elements is aggregated from the Lagrangian elements onto the Eulerian ocean grid (see Section 2.3), and is used to find the surface pressure and ice draft (part of an ice column submerged into the ocean). The ice draft calculated without the aggregation (treating elements as point masses) contains large resolution-dependent

grid artifacts (Figures 7b). These grid artifacts are much reduced after the mass-spreading aggregation is used (Figure 7c).

3.3 Ocean model setup

The KID model is coupled to the MOM6 ocean model [Hallberg et al, 2013]. The ocean model configuration uses a vertical coordinate system which is a hybrid between a sigma-level and a z-level coordinate. In particular, model layers deform underneath the ice shelf as they would in a sigma-coordinate model, but collapse to zero thickness when they intersect with bottom topography, as they would in a z-level model. The coordinate system was achieved using the ALE regridding-remapping scheme [White et al, 2009]. The model uses a horizontal resolution of 2 km, and 72 vertical layers. All simulations were repeated using the ocean model configured in isopycnal mode (results were similar and are not presented here).

Ocean parameters are as specified in the MISOMIP configuration [Asay-Davis et al, 2016], and are shown in Table 1. The simulation is initially at rest, with horizontally uniform initial ocean temperature and salinity profiles which vary linearly between specified surface and bottom values: $T_{\text{top}} = -1.9°$ C, $T_{\text{bottom}} = 1.0°$ C, $S_{\text{top}} = 33.8$ psu, $S_{\text{bottom}} = 34.7$ psu. The maximum ocean depth is $H_{\text{ocean}} = 720$ m. A sponge layer is used on the northern boundary of the domain, which relaxes the temperature and salinity back to the initial temperature and salinity profile. The sponge layer has length $L_{\text{sponge}} = 10$ km, and has a relaxation time scale parameter $T_{\text{sponge}} = 0.1$ days at the northern boundary. The inverse of the relaxation time scale parameter drops linearly to zero over the length of the sponge layer. Melting is set to zero for ocean cells where the ocean column thickness is less than 10m to avoid using more energy to melt ice than is present in the water column.

3.4 Spinup period

The model is spun up for 5 years with all ice elements being fixed. During spinup, the injection of buoyant meltwater at the base of the ice shelf drives a clockwise circulation within the domain (not shown). The circulation compares well with an identical static ice-shelf experiment run using an Eulerian ice-shelf model [Goldberg et al, 2012]. A detailed comparison of the Lagrangian and Eulerian ice-shelf models will be presented in a separate study, and is not shown here.

3.5 Iceberg calving

After spinup, a large tabular iceberg detaches from the ice shelf, and is allowed to drift into the open ocean. Since the focus of this study is on developing a framework for modeling tabular icebergs, we bypass the question of how to prescribe a physical calving law [Benn et all, 2007; Alley et al, 2008; Levermann et al, 2012; Bassis and Jacobs, 2013] by manually breaking off a semi-circular iceberg. This is achieved by allowing all ice elements initially within a 14.4 km radius of the center of the ice front to move freely while the other ice elements continue to be held stationary. Ice elements less than 12 km from the center of the ice front, are bonded together to form a semi-circular tabular iceberg. A ring of elements whose distance, d, from the ice front center obeys 12 km $\leq d \leq$ 14.4 km, are allowed to move freely, but have all their bonds removed. Elements in this half annulus represent fragments of the ice shelf which calve into small pieces during the calving event.

After the spinup period, a wind stress $\vec{\tau} =< \tau_x, \tau_y >=< 0.05, 0.05 > \frac{N}{m^2}$ is applied to drive the tabular iceberg away from the ice-shelf cavity. This is referred to as the Control simulation. Perturbation experiments were also performed using other wind

stress values. Further perturbation experiments were performed by breaking some numerical bonds in order to break the tabular iceberg into smaller pieces.

4 Model Results

After spinup of the Control simulation, the elements near the ice-shelf front are allowed to move freely, and the icebergs begin to drift away from the ice shelf while fully submerged in the ocean (see Figures 2 and 8, and the movie S1 in the Supporting Information). At this point, the iceberg model and the ocean model are fully coupled: changes to the iceberg position alter the top-of-ocean pressure and dynamical boundary condition; and changes to the iceberg melt rates alter the top-of-ocean temperature, salt and mass fluxes. These changing ocean boundary conditions influence the ocean by triggering gravity waves, driving surface mixing, and affecting the ocean stratification. The evolving ocean velocities, temperatures and salinities feedback onto the ice elements by changing the force balance on the ice elements (leading to changes in the elements' position), and altering the melt rates. The various feedbacks within this coupled system offer many opportunities for the model to become unstable. The fact that the model is stable and that we are able to simulate tabular icebergs moving in the ocean without the model crashing and introducing artificial effects like tsunamis, is a non-trivial technical milestone.

4.1 Iceberg motion

In the Control simulation, the semi-circular tabular iceberg moves as a cohesive unit due to the presence of the numerical bonds, while the smaller ice fragments quickly disperse (Figure 2). The tabular iceberg drifts towards the north east, driven by the wind and steered by the Coriolis force. As the tabular iceberg drifts northwards, it rotates in a counterclockwise direction (the direction of the Coriolis force in the Southern Hemisphere), and makes contact with the eastern boundary of the domain, before continuing northward. Most of the smaller ice fragments also move to the northeast, but not as a cohesive unit. Some of these element also move to other parts of the domain.

The direction (and speed) of the iceberg drift is largely determined by the wind speed and direction. Perturbation experiments using different wind stresses show that for sufficiently large winds, the tabular iceberg drifts to the north east when $\tau_x > 0$, and to the north west when $\tau_x < 0$ (not shown). For a purely zonal wind stress with $|\tau_x| \leq 0.01 \frac{N}{m^2}$, the iceberg does not move away from the ice shelf. When the wind is purely offshore ($\tau_x = 0.0 \frac{N}{m^2}$), a meridional wind stress $\tau_y \geq 0.05 \frac{N}{m^2}$ is needed to move the tabular iceberg away from the ice shelf. While this result is partly an artifact of the chosen shape of the calving iceberg, it is also consistent with Bassis and Jacobs [2013] who noted that calving is a two step process consisting of (i) ice-shelf rifting that forms an iceberg and (ii) iceberg detachment. The results here suggest that strong (cross-shore) winds may be required to drive large tabular icebergs away from their source ice shelves.

4.2 Breaking bonds

The numerical bonds in the iceberg model enable the tabular iceberg to retain its shape. This is demonstrated by comparing the Control simulation to an identical simulation where all numerical bonds have been removed (Figure 9, movie S5). In the bond-free simulation, the ice elements disperse and the calved iceberg quickly loses its original structure. This bond-free simulation does not adequately represent the tabular iceberg, since a tabular iceberg needs to be able to move long distances through the ocean as a cohesive unit. This result motivates the inclusion of bonds in the iceberg model, even though they are more computationally expensive than traditional point-iceberg models.

By breaking some (but not all) numerical bonds, we can simulate breaking of tabular icebergs into smaller pieces. Figure 10 shows the results of an experiment which is

–12–

identical to the Control experiment, except that all numerical bonds that intersect the line $x = \frac{L_x}{2}$ have also been severed. This effectively cuts the large tabular iceberg into two halves. As the icebergs drift northwards, the two halves of the tabular iceberg each move as a cohesive unit, but they are able to move independently of one other (Figure 10, movie S2). The two large fragments initially move together, but begin to separate after a few days. The breaking of a tabular iceberg has the additional effect of increasing the total surface area of ice exposed to the ocean, thus increasing the total decay rate of the icebergs.

4.3 Ocean response

Since the tabular iceberg is submerged in the ocean, the iceberg calving and drift affects the surrounding ocean. In the Control simulation, as the tabular iceberg drifts northward a warming of the surface waters is observed around the tabular iceberg, with the largest warming occurring at the ice-shelf front and along the tabular iceberg's rounded edge (Figure 2). This surface warming is caused by upwelling of the warmer waters from beneath the ice shelf and iceberg. As the iceberg drifts away from the ice shelf, these warmer waters remain at the surface, mapping out the iceberg wake (Figure 2). The motion of the tabular iceberg disturbs the ocean surface, which affects ocean velocities through out the water column (Figure 11). The elevated shears around the tabular iceberg lead to increased vertical mixing in the vicinity of the iceberg, which alters the stratification of the water column (Figure 8), warming the upper ocean. The signature of upwelling water in the wake of a drifting tabular iceberg bears some similarity to satellite observations of streaks of increased ocean color in the wake of tabular iceberg in the Southern Ocean [Duprat et al, 2016], suggesting that the increased productivity around icebergs may be driven by upwelling water delivering nutrients to the surface.

The surface warming and increased ocean mixing observed around the iceberg are in contrast to the cooling of the ocean surface and increased stratification reported around melting icebergs in previous modeling studies using point-particle icebergs [Martin and Adcroft, 2010; Stern et al, 2016; Marsh et al, 2015]. This difference results from the fact that in our model the iceberg is submerged in the ocean and extends across an area covering multiple grid cells. This allows the ocean circulation below the iceberg to be resolved, and in this case, for upwelling to occur which warms the ocean surface. In contrast, levitating point-particle iceberg models used in global climate simulation do not resolve the flow beneath the icebergs. In these models, the icebergs only influence the ocean via surface freshwater fluxes (applied at a single point), which cool and stratify the ocean mixed layer. In general the sea surface temperature response to the presence of an iceberg submerged in the water column will likely depend on multiple factors such as the ambient stratification around the iceberg, the amount of melting beneath the iceberg, the amount of entrainment into the iceberg meltwater plume, the geometry of the iceberg, local winds, topography and ocean currents, and the relative motion of the iceberg and the ocean. Further work is required to determine whether the presence of tabular icebergs in the Southern Ocean leads to a net warming or cooling of the ocean surface. This result could have important implications, since the warming/cooling of surface waters around icebergs can lead to large-scale changes to sea-ice concentrations and dense-water production [Stern et al, 2016].

4.4 Iceberg melt rates

The increased subsurface velocities and temperatures cause elevated melt rates at the base of the ice shelf and iceberg (Figure 12). The largest melt rates are observed at the newly calved ice-shelf front and on the rounded side of the tabular iceberg (Figure 12a), where the iceberg calving has created steep ice cliffs. These sharp ice fronts allow for large ocean currents (Figure 12c), which drive the elevated melt rates. The elevated melt rates act to smooth out the ice front over time, making the ice cliff less steep. While

this is likely a real phenomenon that could be observed in nature, we should be wary of the modeled velocities at the ice cliffs, since large changes in ice thicknesses are associated with numerical pressure gradient errors which can drive spurious motion.

The large melt rates along the ice edges are also partly driven by the fact that different melt parametrization are used in the interior and edges of large ice structures (see Section 2.5). Figure 13 shows the melt rates computed with (a) the 3-equation-model parametrization [Holland and Jenkins, 1999], (b) point-particle-iceberg-melt parametrization [Gladstone et al, 2001], and (c) the mixed-melt-rate parametrization (introduced in Section 2.5). The 3-equation-model melt rates (Figure 13a) are less than a third of the size of those calculated using the point-particle-iceberg-melt parametrization (Figure 13b). The point-particle-iceberg-melt is dominated by the wave erosion term, which is an order of magnitude larger than the basal melt. When the mixed-melt-rate parametrization is used (Figure 13c), the very high melt rates are only observed at the edges of ice structures.

5 Summary

In this study we present a novel framework for simulating tabular icebergs in ocean models, and representing icebergs with finite extent and structure submerged in the ocean. In this framework, large tabular icebergs are represented by collections of Lagrangian elements that are held together by numerical bonds. Each ice element is assigned a surface area and shape, and can interact with the ocean and other elements in a way which is consistent with the shape of the element. Such a representation allows tabular icebergs to interact with the ocean across a wide area (larger than a grid cell), and individual ice elements to behave as if they had a finite extent. This is in contrast to previous representations of icebergs in numerical models [Jongma et al, 2009; Martin and Adcroft, 2010; Marsh et al, 2015] that treat icebergs as point particles. Assigning a finite extent to elements prevents icebergs from piling up on top of one another, which has been an issue for previous point-particle iceberg models. Explicitly resolving tabular icebergs in the ocean allows the icebergs to apply pressure to the ocean surface and thus to interact with the ocean in a more realistic way, and allows us to study the effects that tabular icebergs have on ocean circulation. Including numerical bonds between elements allows for simulations which emulate iceberg calving and fracture by severing the bonds.

The capabilities of the tabular iceberg model are demonstrated by modeling a tabular iceberg drifting away from an idealized ice shelf (also constructed using Lagrangian elements). The results show that explicitly resolving tabular icebergs in the ocean allows for a complex interaction between the iceberg and the surrounding ocean. In our Control setup, a tabular iceberg is driven away from the ice shelf by ocean currents, wind stress, and the Coriolis force. As the iceberg moves through the water, it disturbs the ocean surface, driving ocean currents. The motion of the iceberg and melt beneath the iceberg drive upwelling along the sides of the iceberg, which entrains ambient water and causes a warming of the surface ocean in the wake of the iceberg. The changing ocean conditions feed back onto the iceberg, affecting its motion and melt rates. The highest melt rates are observed at the edge of the iceberg which has the steepest ice cliff. These have the effect of smoothing out the ice edge over time. Simulations without using numerical bonds show that the bonds are essential for allowing the iceberg to move as a unit. We also demonstrate that by breaking these numerical bonds we can simulate iceberg fracture, which is an important process that increases the rate of iceberg decay.

To our knowledge, the model presented in this study is the first model to explicitly resolve drifting tabular icebergs in an ocean model that can be used for climate studies. A natural extension of this work is a representation of tabular icebergs in a general circulation model (GCM). However, before this can be done, there are a number of issues that need to be resolved: firstly, the question of how and when to introduce tab-

ular icebergs into the ocean needs to be addressed [Stern et al, 2016]. For GCMs with active ice shelves, a calving law is needed to release the tabular iceberg into the ocean. The question of what calving law to use is a topic of ongoing research [Benn et all, 2007; Alley et al, 2008; Levermann et al, 2012; Bassis and Jacobs, 2013] and is still unresolved. One potential way to temporarily bypass this problem would be to run hindcast simulations using historically observed calving events. A related issue is the question of how and when to break the bonds within the freely floating icebergs to simulate iceberg breakup. Without a rule for iceberg breakup, the tabular icebergs would likely drift to unrealistically low latitudes. Further work is also needed to understand (and model) the interactions between tabular icebergs and sea ice, and to parametrize the effects of iceberg grounding, as these interactions play a large role in dictating the trajectories of tabular icebergs. However, despite these remaining challenges, the technical framework described in this article is potentially a useful step towards including tabular icebergs in global GCMs.

6 Appendix A

6.1 Environmental forces on ice elements

The non-interactive forces on an ice element are as described in [Martin and Adcroft, 2010], with a small modification to drag forces and wave radiation force, included to account for elements which are part of larger ice structures, and have a reduced surface area exposed to the ocean. When modeling the momentum balance, the elements are assumed to be cuboids with time-evolving lengths, widths and thicknesses. The length L and width W of an element are initially set to $L = W = \sqrt{A_s}$, and thereafter evolve dynamically. A_s is the planar surface area of the element. The cuboid shape is used so that the momentum balance of unbonded elements is exactly as described in [Martin and Adcroft, 2010]. The mismatch between the cuboid shape used in the momentum balance and the hexagonal shape used for spreading mass onto the ocean grid introduces a small error. This error is likely to be small compared to the uncertainty in the drag coefficients, melt parametrization and other uncertainties built into a iceberg model.

The forces on an element due to air (a), ocean (o) and sea ice (si) drag are given by

$$(\vec{F}_a) = \rho_a(0.5c_{a,v}WF + \epsilon c_{a,h}LW)|\vec{u}_a - \vec{u}|(\vec{u}_a - \vec{u}), \tag{11}$$

$$(\vec{F}_o) = \rho_o(0.5c_{o,v}W(D - T_{si}) + \epsilon c_{o,h}LW)|\vec{u}_o - \vec{u}|(\vec{u}_o - \vec{u}), \tag{12}$$

$$(\vec{F}_{si}) = \rho_{si}(0.5c_{si,v}WT_{si}F + \epsilon c_{si,h}LW)|\vec{u}_{si} - \vec{u}|(\vec{u}_{si} - \vec{u}). \tag{13}$$

Here ρ_a, ρ_o, ρ_{si}, are the density of air, ocean and sea ice, respectively. $c_{a,v}$, $c_{o,v}$ and $c_{si,v}$ are the vertical drag coefficients with air, ocean and sea ice, while $c_{a,h}$, $c_{o,h}$ and $c_{si,h}$ are the respective horizontal drag coefficients. $\vec{u}_a$, $\vec{u}_o$, $\vec{u}_{si}$, are the velocities of air, ocean and sea ice, respectively. L, W, T, F and D are the length, width, thickness, freeboard, and draft of the ice element. L and W are defined such that $L \geq W$. The element thickness is related to the draft and freeboard by $T = F + D$ and $D = \frac{\rho}{\rho_o}T$, where ρ is the ice element density. T_{si} is the sea-ice thickness. As discussed in Section 2.5, ϵ is the fraction of an element's perimeter surrounded by ocean, and is given by $\epsilon = 1 - \frac{N_b}{N_{\max}}$, where $N_{\max}$ is the maximum number of bonds that an element form, and N_b is the number of bonds that the element forms.

The wave radiation force $(\vec{F}_R)$ is given by

$$\vec{F}_R = \epsilon \rho_o c_r ga \, \frac{WL}{W + L} \frac{\vec{u}_a}{|\vec{u}_a|} \, \min(a, F) \tag{14}$$

where g is the acceleration due to gravity, a is the wave amplitude empirically related to the wind speed by $a = 0.010125|\vec{u}_a - \vec{u}_o|$, and c_{wd} is the wave drag coefficient de-

fined as

$$c_{wd} = 0.06 \min\left(\max\left[0, \frac{L - L_c}{L_t - L_c}\right], 1\right),$$ (15)

where $L_w = 0.32|\vec{u}_a - \vec{u}_o|^2$ is an empirical wave length, $L_c = 0.125 L_w$ is the cutoff length, and $L_t = 0.25 L_w$ is the upper limit.

The pressure gradient force is approximated as a force due to sea surface slope and given by

$$\vec{F}_{SS} = -Mg\vec{\nabla}\eta$$ (16)

where η is the sea surface height.

A parametrization for iceberg capsizing is applied for tall narrow ice elements. Elements capsize when the ratio $\frac{W}{H} < \sqrt{6\alpha(1-\alpha)}$, where $\alpha = \frac{\rho}{\rho_o}$. [Wagner et al, 2017]. When this occurs, W and H are instantaneously swapped. The iceberg capsizing parametrization used here is different from the one described in [Martin and Adcroft, 2010], which was found to be inappropriate for modeling icebergs with evolving dimensions [Wagner et al, 2017]. In our model capsizing is only permitted for unbonded elements.

6.2 Melt rate parametrization

As discussed in Section 2.5, unbounded ice elements in the iceberg model decay according to parameterizations for iceberg decay typically used in iceberg drift models [Martin and Adcroft, 2010], while ice elements within larger ice structures have only a basal melt given by the three equation model [Holland and Jenkins, 1999]. For the purposes of applying melt rates, we again assume that the elements are cuboids with time-evolving lengths, widths and thicknesses, as discussed in the previous subsection above.

For unbonded ice elements, the element thickness decays due to basal melt at a rate M_b, while the length and width of the elements decay as a result of wave erosion, M_e, and melt due to buoyant convection, M_v. Following Gladstone et al [2001] and Martin and Adcroft [2010], the basal melt rate, the 'melt' due to wave erosion, and buoyant convection melt rate are parameterized by

$$M_b = 0.58|\vec{u} - \vec{u}_o|^{0.8}\frac{\tilde{T}_o - \tilde{T}}{L^{0.2}}$$ (17)

$$M_e = \frac{1}{12}S_s\left(1 + \cos\left[\pi A_i^3\right]\right)\left(\tilde{T}_o + 2\right),$$ (18)

$$M_v = \left(7.62 \times 10^{-3}\right)\tilde{T}_o + \left(1.29 \times 10^{-3}\right)\tilde{T}_o^2.$$ (19)

$\tilde{T}$ is the effective iceberg temperature and is set to $\tilde{T} = -4°C$, $\tilde{T}_o$ is the temperature at the top of the ocean, A_i is the sea-ice area fraction, and S_s is the sea state, which is given by the Beaufort scale

$$S_s = \frac{2}{3}|\vec{u}_a - \vec{u}_o|^{\frac{1}{2}} + \frac{1}{10}|\vec{u}_a - \vec{u}_o|$$ (20)

All three melt rates are in units of meters per day.

For elements inside larger structures, the melt due to wave erosion and melt due to buoyant convection are set to zero, and the basal melt, M_s, is given by the standard three equation model [Holland and Jenkins, 1999]: neglecting the heat flux in the ice, the heat flux balance, salt flux balance and freezing point constraint at the ice-ocean interface can be expressed as

$$LM_s = c_{po}\gamma_T|\vec{u}_o - \vec{u}|\left(T_o - T_b\right),$$ (21)

$$S_b M_s = \gamma_S |\vec{u}_o - \vec{u}| \left(S_o - S_b \right) \tag{22}$$

and

$$f(S_b \ , \ T_b \ , \ p_b) = 0. \tag{23}$$

Here T_o and S_o are the boundary-layer temperature and salinity below the ice; T_b, S_b and p_b are the temperature, salinity and pressure at the ice-ocean interface. $c_{po} = 3974$ J kg^{-1} $^\circ$C^{-1} is the specific heat of water, and $L = 3.35\times10^5$ J kg^{-1} is the latent heat of ice fusion. γ_T and γ_S are the coefficients representing the transfer of heat and salt through the boundary layer. The specific formulation of γ_T and γ_S can be found in [Holland and Jenkins, 1999]. The final equation is a constraint imposed by the equation of state, which relates the pressure-dependent freezing temperature and salinity at the ice-ocean interface. The basal melt rate M_s is found by numerically solving this system of three equations.

7 Appendix B

7.1 Modified Verlet Algorithm

The model uses a version velocity Verlet time-stepping algorithm, which has been modified to allow part of the forcing to be calculated implicitly. The traditional velocity Verlet algorithm is commonly used in molecular dynamics, as it is simple to implement, second order accurate and computationally efficient [Swope et al, 1982; Omelyan et al, 2002]. Here we modify the traditional scheme to allow for the drag forces to be modeled implicitly, which prevents large accelerations for elements whose mass approaches zero. To do this, we include both an implicit and explicit acceleration, $\vec{a} = \vec{a}^{\mathrm{exp}} + \vec{a}^{\mathrm{imp}}$. The explicit acceleration, $\vec{a}^{\mathrm{exp}}$, includes all forcing terms which depend only on the previous time step and the current position, while the implicit acceleration, $\vec{a}^{\mathrm{imp}}$, includes forcing terms which depend on the velocity at the current time step (in particular the drag and Coriolis forces).

Using a time step of Δt, and subscripts to denote the time step (so that $t_{n+1} = t_n + \Delta t$), the modified velocity Verlet scheme can be written as:

1) Calculate updated position: $\vec{x}_{n+1} = \vec{x}_n + \vec{u}_n \Delta t + \dfrac{\Delta t^2}{2} \left(\vec{a}_n^{\mathrm{exp}} + \vec{a}_n^{\mathrm{imp}} \right)$.

2) Calculate $\vec{a}_{n+1}^{\mathrm{exp}}$

3) Calculate $\vec{a}_{n+1}^{\mathrm{imp}}$ and $\vec{u}_{n+1} = \vec{u}_n + \dfrac{\Delta t}{2} \left(\vec{a}_n^{\mathrm{exp}} + \vec{a}_{n+1}^{\mathrm{exp}} \right) + (\Delta t)\vec{a}_{n+1}^{\mathrm{imp}}$

This scheme reduces to the traditional velocity Verlet when $\vec{a}^{\mathrm{imp}}$ is set to zero. Note that $\vec{a}_{n+1}^{\mathrm{exp}} = \vec{a}_{n+1}^{\mathrm{exp}}(\vec{x}_{n+1}, t_n)$ is an explicit function of $\vec{x}_{n+1}$ and other quantities evaluated at time t_n, while $\vec{a}_{n+1}^{\mathrm{imp}} = \vec{a}_{n+1}^{\mathrm{imp}}(\vec{u}_{n+1}, \vec{x}_{n+1}, t_n)$ additionally depends on u_{n+1}, and needs to be solved implicitly. For this reason in step three, $\vec{a}_{n+1}^{\mathrm{imp}}$ and $\vec{u}_{n+1}$ need to be solved simultaneously, as described in the next subsection.

In equation (1), the forces due to ocean drag, atmospheric drag and sea ice drag are treated implicitly. The force due to sea surface slope and wave radiation are treated explicitly. The Coriolis term is handled using the Crank-Nicolson scheme so that half of the effect is implicit and half is explicit. The elastic part of the interactive forces is treated explicitly, while the interactive damping is handled semi-implicitly in that the drag force on element A by element B depends on the velocities of elements A and B evaluated at time t_{n+1} and t_n, respectively.

7.2 Solving for the velocity implicitly

Since this modified scheme contains some forcing terms which are handled implicitly, $\vec{a}_{n+1}^{\text{imp}}$ and $\vec{u}_{n+1}$ need to be calculated simultaneously. We demonstrate how this is done, using a simplified one-dimensional version of equation (1), neglecting the atmospheric drag, sea-ice drag and Coriolis force, so that the only implicitly treated term is the ocean drag. In this demonstration, we use a superscript to denote the ocean drag force, F^o, and ocean velocity, u^o, to avoid confusion with the subscripts indicating time step. We also define an explicit force, F^{exp}, which accounts for all forces not proportional to the element velocity. With these simplifications, the implicit and explicit accelerations are

$$a^{\text{exp}} = \frac{1}{M}(F^{\text{exp}}) \tag{24}$$

$$a^{\text{imp}} = \frac{1}{M}(F^o) \tag{25}$$

The ocean drag force at time t_{n+1} is modeled (mostly) implicitly as

$$F^o_{n+1} = \tilde{c}^o |u^o_n - u_n|(u^o_n - u_{n+1}), \tag{26}$$

where $\tilde{c}^o$ is the effective drag coefficient, accounting for the dimensions of the ice element (see equation 12).

Step 3 of the modified velocity Verlet scheme can be rewritten by introducing an intermediate velocity u^*, which only depends on the velocity and acceleration at time t_n,

$$u^*_n = u_n + \frac{1}{2}(\Delta t)a_n^{\text{exp}}. \tag{27}$$

Using this, the updated velocity (Step 3) can be written

$$u_{n+1} = u^*_n + \frac{\Delta t}{2}a_{n+1}^{\text{exp}} + (\Delta t)a_{n+1}^{\text{imp}}. \tag{28}$$

Including the forcing terms into this equations gives

$$u_{n+1} = u^*_n + \frac{\Delta t}{2M}(F_{n+1}^{\text{exp}}) + \frac{\Delta t}{M}\left(c_w|u^o_n - u_n|(u^o_n - u_{n+1})\right) \tag{29}$$

Solving for $u(t_{n+1})$ in terms of quantities which only depend on the previous time step gives

$$u_{n+1} = \frac{u^*_n + \frac{\Delta t}{2M}(F_{n+1}^{\text{exp}}) + \frac{\Delta t}{M}\left(c_w|u^o_n - u_n|(u^o_n)\right)}{\left(1 + \frac{\Delta t}{M}c_w|u^o_n - u_n|\right)} \tag{30}$$

Recall that F_{n+1}^{exp} is an explicit function of x_{n+1} and other quantities evaluated at t_n, which are already known at this point. Once the u_{n+1} has been found, it can be used to calculate the explicit and implicit accelerations, which are required for the next time step.

Finally, we note that the the drag term (equation 26) is not entirely implicit, since the element velocity inside the absolute value is evaluated at time t_n, rather than at time t_{n+1}. This is done so that we can solve for the updated velocity analytically. One consequence of this is that it can give rise to a small oscillation in the element velocity. This oscillation is addressed by using a predictive corrective scheme: after solving for a first guess of the velocity at time t_{n+1}, this estimate of the velocity is used to update the estimate of the drag force (i.e.: inside the absolute value signs). This updated drag can now be used to repeat the process described above to find an improved estimate of the

velocity. We found that two iterations were sufficient to remove the unwanted oscillation.

The procedure described in this section is easily extended to include more forcing terms and two dimensions (where it involves inverting a 2×2 matrix).

8 Appendix C

Connecting bonds across processor boundaries
Since the model is parallelized across multiple distributed-memory processors, it often happens that two elements on different processes are bonded together. Keeping track of numerical bonds across processor boundaries requires a lot of book keeping. In this section we describe how the model handles bonds across processor boundaries.

The basics of the bond bookkeeping work as follows: consider an element A and an element B that are bonded together. Each element has a copy of the bond (a piece of memory which describes the bond between the two elements), which is stored with the element. Let A-B be the bond stored by element A, and B-A be the bond stored by element B. Bond A-B contains a pointer which points to element B and bond B-A contains a pointer which points to element A.

Consider a situation where element A and B are originally on Processor 1, and then element B moves to Processor 2. When this occurs, the memory assigned to element B on processor 1 is removed, and is allocated on Processor 2. This means that the pointer to element B in bond A-B (stored in element A on Processor 1) is no longer assigned. Similarly, the pointer to element A in bond B-A (stored in element B on Processor 2) is no longer assigned. Before the next time step, a halo update occurs, so that the there is a copy of element A in the halo of Processor 2 and a copy of element B in the halo of Processor 1. After the halo update, the bonds A-B and B-A have to be reconnected on both Processor 1 and 2. To aid in reconnecting the bonds, a copy of the grid cell number of element B is stored in the bond A-B and a copy of the grid cell number of element A is stored in the bond B-A. We refer to this as the 'most recent address'. Before a bond is moved from one processor to another, the 'most recent address' is updated, so that the bond can be reconnected later. To reconnect bond A-B on Processor 1 (for example), we find the most recent address of element B, and search through the list of elements in the grid cell corresponding to the most recent address of element B until element B is found. The pointer to element B in bond A-B is reassigned, and the bond is said to be connected.

References

Asay-Davis, X. S., S. L. Cornford, B. K. Galton-Fenzi, R. M. Gladstone, G. H. Gudmundsson, D. M. Holland, P. R. Holland, and D. F. Martin (2016), Experimental design for three interrelated marine ice sheet and ocean model intercomparison projects: MISMIP v. 3 (MISMIP+), ISOMIP v. 2 (ISOMIP+) and MISOMIP v. 1 (MISOMIP1). *Geoscientific Model Development* 9, no. 7: 2471.

Arrigo, K. R., G. L. van Dijken, D. G. Ainley, M. A. Fahnestock, and T. Markus (2002). Ecological impact of a large Antarctic iceberg. *Geophys. Res. Let.*, 29(7).

Alley, R. B., H. J. Horgan, I. Joughin, K. M. Cuffey, T. K. Dupont, B. R. Parizek, S. Anandakrishnan, and J. Bassis (2008), A simple law for ice-shelf calving. *Science* 322, no. 5906, 1344-1344.

Bassis, J. N., and S. Jacobs (2013), Diverse calving patterns linked to glacier geometry. *Nature Geoscience*, 6(10), 833-836.

Benn, D. I., C. R. Warren, and R. H. Mottram (2007). Calving processes and the dynamics of calving glaciers. *Earth-Science Reviews*, 82(3), 143-179.

Bigg, G. R., Wadley, M. R., Stevens, D. P., and Johnson, J. A. (1997), Modeling the dynamics and thermodynamics of icebergs. *Cold Regions Science and Technology*, 26(2), 113-135.

Borstad, C. P., A. Khazendar, E. Larour, M. Morlighem, E. Rignot, M. P. Schodlok, and H. Seroussi (2012), A damage mechanics assessment of the Larsen B ice shelf prior to collapse: Toward a physically-based calving law, *Geophys. Res. Lett.*, 39, L18502

Biddle, L. C., J. Kaiser, K. J. Heywood, A. F. Thompson and A. Jenkins (2015), Ocean glider observations of iceberg-enhanced biological productivity in the northwestern Weddell Sea, *Geophys. Res. Lett.*, 42, 459465.

Cundall, P. A and O. D. L. Strack (1979), A discrete numerical model for granular assemblies. *Geotechnique* 29, pp. 4765

De Rydt, J., and G. H. Gudmundsson (2016), Coupled ice shelf ocean modeling and complex grounding line retreat from a seabed ridge. *J. of Geophys. Res.: Earth Surface*, 121(5), 865-880.

Dunne, J.P., J.G. John,, A.J. Adcroft, S.M. Griffies, R.W. Hallberg, E. Shevliakova, R.J. Stouffer, W. Cooke, K.A. Dunne, M.J Harrison, and J.P. Krasting (2012), GFDL's ESM2 global coupled climate-carbon Earth System Models. Part I: Physical formulation and baseline simulation characteristics. *J. of Climate*, 25(19), 6646-6665.

Depoorter, M. A., J. L. Bamber, J. A. Griggs, J. T. M. Lenaerts, Stefan RM Ligtenberg, M. R. van den Broke, and G. Moholdt (2013), Calving fluxes and basal melt rates of Antarctic ice shelves. *Nature*, 502(7469), 89-92.

Determan J., Gerdes R. (1994), Melting and freezing beneath ice shelves: implications from a three-dimensional ocean-circulation model. *Ann. Glaciol.*, 20, 413-419.

Dowdeswell, J. A., and J. L. Bamber (2007), Keel depths of modern Antarctic icebergs and implications for sea-floor scouring in the geological record. *Marine Geology*, 243(1), 120-131.

Duprat, L. P., G. R. Bigg, and D. J. Wilton (2016), Enhanced Southern Ocean marine productivity due to fertilization by giant icebergs. *Nature Geoscience.*

Eckert, E. R. G. (1950). Introduction to the Transfer of Heat and Mass. McGraw-Hill.

Fogwill, C.J., E. van Sebille, E.A. Cougnon, C.S. Turney, S.R. Rintoul, B.K. Galton-Fenzi, G.F. Clark, E.M. Marzinelli, E.B. Rainsley, and L. Carter (2016), Brief communication: Impacts of a developing polynya off Commonwealth Bay, East Antarctica, triggered by grounding of iceberg B09B. *The Cryosphere*, 10(6), p.2603.
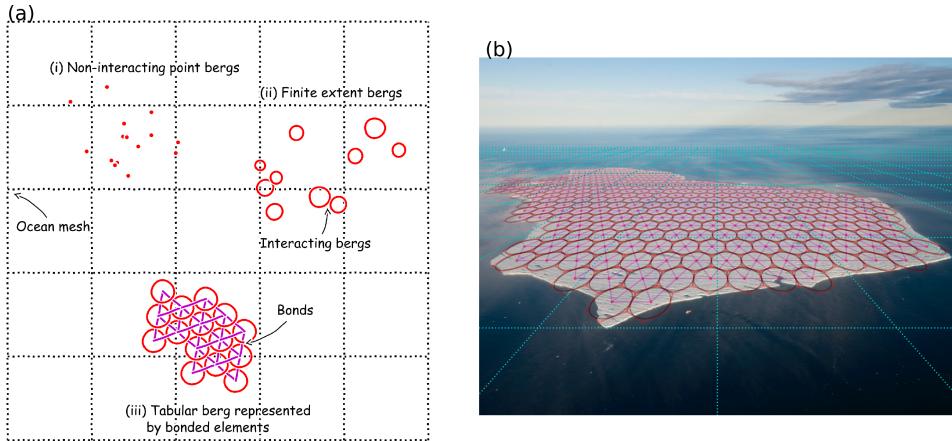
Gladstone, R. M., G. R. Bigg, and K. W. Nicholls. (2001), Iceberg trajectory modeling and meltwater injection in the Southern Ocean (19782012). *J. of Geophys. Res.: Oceans*, 106(C9), 19903-19915.

Goldberg, D. N., C. M. Little, O. V. Sergienko, A. Gnanadesikan, R. Hallberg, and M. Oppenheimer (2012), Investigation of land ice?ocean interaction with a fully coupled ice-ocean model: 1. Model description and behavior. *J. of Geophys. Res.: Earth Surface*, 117(F2).

Gladish, C. V., D. M. Holland, P. R. Holland, and S. F. Price (2012), Ice-shelf basal channels in a coupled ice/ocean model. *J. of Glaciol.*, 58(212), 1227-1244.

Grosfeld K., R. Gerdes, J. Determan (1997), Thermohaline circulation and interaction between ice shelf cavities and the adjacent open ocean. *J. Phys. Oceanogr.*, **102**, C7, 15959-15610.

Grosfeld, K., and H. Sandhger, (2004). The evolution of a coupled ice shelfocean system under different climate states. *Global and Planetary Change*, 42(1), 107-132.

Hallberg, R., A. Adcroft, J. P. Dunne, J. P., Krasting, R. J., and Stouffer (2013), Sensitivity of twenty-first-century global-mean steric sea level rise to ocean model formulation. J. of Climate, 26(9), 2947-2956.

Holland D. M., Jenkins A. (2001), Adaptation of an isopycnic coordinate ocean model for the study of circulation beneath ice shelves. *Mon. Wea. Rev.*, 129, 1905-1927.

Holland P. R. and D. L. Feltham (2006), The effects of rotation and ice shelf topography on frazil-laden Ice Shelf Water plumes. *J. Phys. Oceanogr.*, 36, 2312-2327.

Holland, D. M., and A. Jenkins (1999), Modeling thermodynamic ice-ocean interactions at the base of an ice shelf. J. of Phys. Oceanogr. 29.8, 1787-1800.

Hellmer H.H., Olbers D. J. (1989), A two-dimensional model for the thermohaline circulation under an ice shelf. *Antarctic Science*, 1, 325- 336.

Henderson J., J. S. P. Loe (2016), The Prospects andChallenges for Arctic Oil Development. *Oil, Gas and Energy Law Journal (OGEL)*, 14 (2)

Hopkins, M. A. (1996). On the mesoscale interaction of lead ice and floes. *J. of Geophys. Res.: Oceans*, 101(C8), 18315-18326.

Hopkins, M. A. (2004). A discrete element Lagrangian sea ice model. *Engineering Computations*, 21(2/3/4), 409-421.

Hunke, Elizabeth C., and Darin Comeau (2011), Sea ice and iceberg dynamic interaction. *J. of Geophys. Res.: Oceans* 116, C5.

Gaskill, H. S., and J. Rochester (1984). A new technique for iceberg drift prediction. *Cold Reg. Sci. Technol.*, 8(3), 223-234.

Jacobs, S. S., H. H. Helmer, C. S. M. Doake, A. Jenkins, R. M. Frolich (1992), Melting of ice shelves and the mass balance of Antarctica. *J. of Glaciol.*, 38(130), 375-387.

Jakobsen, T. (2001). Advanced character physics. *In Game Developers Conference*, Vol. 3.

Jenkins, A., P. Dutrieux, S. S. Jacobs, S. D. McPhail, J. R. Perrett, A. T. Webb, and D. White (2010), Observations beneath Pine Island Glacier in West Antarctica and implications for its retreat. it Nature Geo., 3(7), 468-472.

Jacobs, S. S., A. Jenkins, C. F. Giulivi, and P. Dutrieux (2011). Stronger ocean circulation and increased melting under Pine Island Glacier ice shelf. Nature Geo., 4(8), 519-523.

Jongma, J. I., E. Driesschaert, T. Fichefet, H. Goosse, and H. Renssen (2009), The effect of dynamic-thermodynamic icebergs on the Southern Ocean climate in a three-dimensional model, *Ocean Modell.*, 26, 104113.

Kubat I., M. Sayed, S. Savage, T. Carrieres (2005), An operational model of iceberg drift *Int. J. Off. Polar Eng.*, 15 (2), 125131

Lewis E.L. and R.G. Perkin (1986), Ice pumps and their rates. *J. of Geophys. Res.*, 91, 11756-11762.

Losch, M. (2008). Modeling ice shelf cavities in a z coordinate ocean general circulation model. *J. of Geophys. Res.: Oceans*, 113(C8).

Li, B., H. Li, Y. Liu, A. Wang and S. Ji (2014), A modified discrete element model for sea ice dynamics. *Acta Oceanologica Sinica*, 33(1), 56-63.

Liu, M. B. and G. R. Liu (2010), Smoothed particle hydrodynamics (SPH): an overview and recent developments. *Archives of computational methods in engineering*, 17(1), 25-76.

Lichey, C., and H. H. Hellmer (2001). Modeling giant-iceberg drift under the influence of sea ice in the Weddell Sea, Antarctica. *J. of Glaciol.*, 47(158), 452-460.

Levermann, A., T. Albrecht, R. Winkelmann, M. A. Martin, M. Haseloff, and I. Joughin. (2012), Kinematic first-order calving law implies potential for abrupt ice-shelf retreat. *The Cryosphere*, 6(2), 273-286.

Luding, S. (2008), Introduction to discrete element methods: basic of contact force models and how to perform the micro-macro transition to continuum theory. *European Journal of Environmental and Civil Engineering* 12.7-8, pp. 785826

Mountain, D. G. (1980). On predicting iceberg drift. *Cold Reg. Sci. Technol.*, 1(3-4), 273-282.

Martin, T., and Adcroft, A. (2010), Parameterizing the fresh-water flux from land ice to ocean with interactive icebergs in a coupled climate model. *Ocean Modelling*, 34(3), 111-124.

Marsh, R., V. O. Ivchenko, N. Skliris, S. Alderson, G. R. Bigg, G. Madec, A. T. Blaker Y. Aksenov, B. Sinha, A.C. Coward, and J.L. Sommer (2015), NEMOICB (v1. 0): interactive icebergs in the NEMO ocean model globally configured at eddy-permitting resolution. *Geoscientific Model Development* 8, no. 5 (2015): 1547-1562.

MacAyeal D.R. (1984), Thermohaline Circulation Below the Ross Ice Shelf: A Consequence of Tidally Induced Vertical Mixing and Basal Melting. *J. Geophys. Res.*, 89, 597-606

Merino, N., Le Sommer, J., Durand, G., Jourdain, N. C., Madec, G., Mathiot, P., and Tournadre, J. (2016), Antarctic icebergs melt over the Southern Ocean: climatology and impact on sea ice. *Ocean Modelling*, 104, 99-110.

Nicholls K.W. (1996), Temperature variability beneath Ronne Ice Shelf, Antarctica, from thermistor cables. *J. Phys. Oceanogr.*, 11, 1199-1210.

Nicholls KW, Østerhus S, Makinson K (2009), Ice-Ocean processes over the continental shelf of the southern Weddell Sea, Antarctica: a review. *Rev. Geophys.* 47(3).

Omelyan, I. P., M. I. Mryglod, and R. Folk (2002), Optimized Verlet-like algorithms for molecular dynamics simulations. *Physical Review E*, 65(5), 056706.

Pizzolato, L., S. E. Howell, C. Derksen, J. Dawson, L. Copland (2014), Changing sea ice conditions and marine transportation activity in Canadian Arctic waters between 1990 and 2012, *Climatic Change* 123 (2), 161173.

Pan, W., A. M. Tartakovsky, and J. J. Monaghan (2013). Smoothed particle hydrodynamics non-Newtonian model for ice-sheet and ice-shelf dynamics. *J. of Comp. Phys.*, 242, 828-842.

Pralong, A., and M. Funk (2005), Dynamic damage model of crevasse opening and application to glacier calving, *J. Geophys. Res.*, 110, B01309.

Rabatel, M., S. Labb and J. Weiss (2015), Dynamics of an assembly of rigid ice floes. J. of Geophys. Res.: Oceans, 120(9), 5887-5909.

Rackow, T., C. Wesche, R. Timmermann, H. H. Hellmer, S. Juricke and T. Jung (2017), A simulation of small to giant Antarctic iceberg evolution: differential impact on climatology estimates. J. of Geophys. Res.: Oceans, doi: 10.1002/2016JC012513

Radjai, F. and F. Dubois (2011), Discrete-Element Modeling of Granular Materials. Wiley-Iste, p. 425
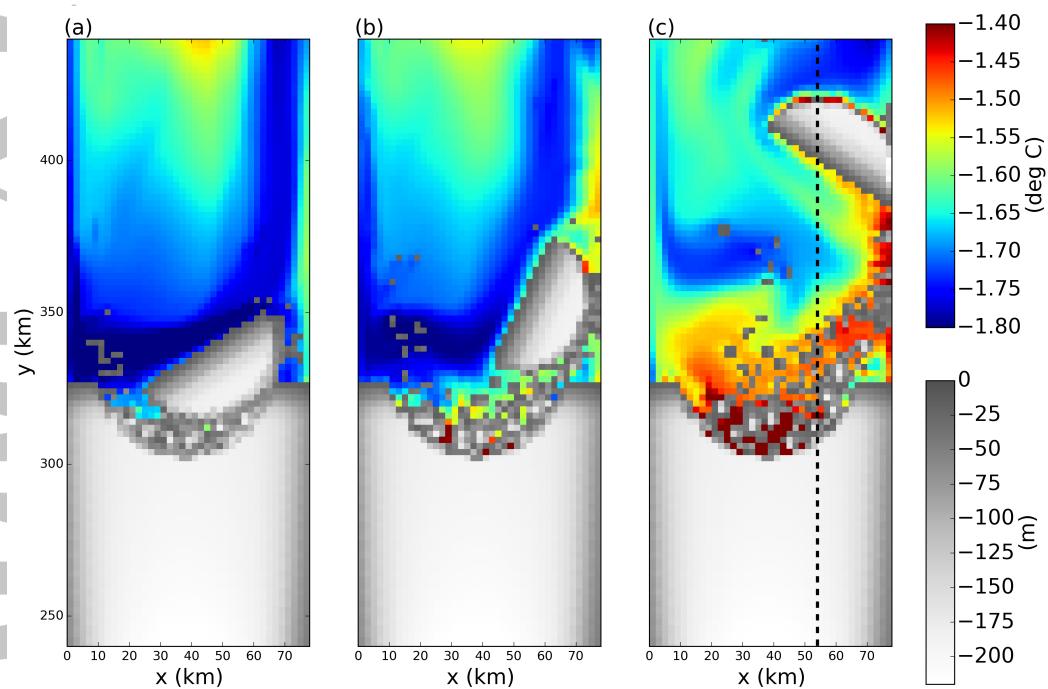
Rignot, E., S. Jacobs, J. Mouginot, and B. Scheuchl (2013), Ice-shelf melting around Antarctica. *Science*, 341, no. 6143 (2013): 266-270.

Robinson, N. J., M. J. M. Williams, P. J. Barrett, and A. R. Pyne (2010), Observations of flow and ice-ocean interaction beneath the McMurdo Ice Shelf, Antarctica, *J. Geophys. Res.*, 115, C03025

Sergienko, O. V. (2013). Basal channels on ice shelves. *J. of Geophys. Res.: Earth Surface*, 118(3), 1342-1355.

Silva, T. A. M., Bigg, G. R., and Nicholls, K. W. (2006), Contribution of giant icebergs to the Southern Ocean freshwater flux. J. of Geophys. Res.: Oceans, 111(C3).

Smith, K., B. Robison, J. Helly, R. Kaufmann, H. Ruhl, H., T. Shaw, and M. Vernet (2007), Free-drifting icebergs: Hotspots of chemical and biological enrichment in the Weddell Sea, *Science*, 317, 478482.

Shepherd, A., and D. Wingham (2007). Recent sea-level contributions of the Antarctic and Greenland ice sheets. *Science*, 315(5818), 1529-1532.

Stern, A., D. M. Holland, P. R. Holland, A. Jenkins and J. Sommeria (2014), The effect of geometry on ice shelf ocean cavity ventilation: a laboratory experiment. *Experiments in Fluids*, 55(5), 1-19.

Stern, A., Johnson, E., Holland, D.M., Wagner, T.J., Wadhams, P., Bates, R., Abrahamsen, E.P., Nicholls, K.W., Crawford, A., Gagnon, J. and Tremblay, J.E. (2015), Wind-driven upwelling around grounded tabular icebergs. *J. of Geophys. Res.: Oceans*, 120(8), 5820-5835.

Stern, A., A. Adcroft, and O. Sergienko (2016), The effects of Antarctic iceberg calving size distribution in a global climate model. *J. of Geophys. Res.: Oceans*, 121(8), 5773-5788.

Swope, W. C., H. C. Andersen, P. H. Berens, and K. R. Wilson (1982), A computer simulation method for the calculation of equilibrium constants for the formation of physical clusters of molecules: Application to small water clusters. *The Journal of Chemical Physics* 76, no. 1, 637-649.

Tournadre, J., N. Bouhier, F. Girard-Ardhuin, and F. Rmy (2016), Antarctic icebergs distributions 1992-2014. *J. Geophys Res: Oceans.*

Turnbull I.D., N. Fournier, M. Stolwijk, T. Fosnaes, D. McGonigal (2015), Operational iceberg drift forecasting in Northwest Greenland, *Cold Reg. Sci. Technol.* 110, 1-18

Unger, J. D., 2014. Regulating the Arctic Gold Rush: Recommended Regulatory Reforms to Protect Alaska's Arctic Environment from Offshore Oil Drilling Pollution . *Alaska L. Rev*, 31

Vernet, M., et al. (2012), Islands of ice: Influence of free-drifting Antarctic icebergs on pelagic marine ecosystems, Oceanography, 25(3), 3839

Wagner., T. J. W., P. Wadhams, R. Bates, P. Elosegui, A. Stern, D. Vella, E. P. Abrahamsen, A. Crawford, and K. W. Nicholls (2014), The footloose mechanism: Iceberg decay from hydrostatic stresses. *Geophys. Res. Let.*, 41(15), 5522-5529.

Wagner, T. J., A. A. Stern, R. W. Dell, and I. Eisenman (2017), On the representation of capsizing in iceberg models. arXiv preprint arXiv:1702.06870.

Weeks, W. F., and W. J. Campbell (1973). Icebergs as a fresh-water source: an appraisal. *J. of Glaciol.*, 12(65), 207-233.

White, L., A. Adcroft, and R. Hallberg (2009), High-order regridding-remapping schemes for continuous isopycnal and generalized coordinates in ocean models. *J. of Comp. Phys.*, 228(23), 8665-8692.

Parameter	Symbol	Value	Unit
Domain Length	L_x	80	km
Domain Width	L_y	480	km
Horizontal Resolution	Δx	2	km
Number of vertical layers	N_l	72	non-dim
Horizontal Viscosity	ν_H	6.0	m^2 s^{-1}
Diapycnal Viscosity	ν_V	10^{-3}	m^2 s^{-1}
Horizontal Diffusivity	ϵ_H	1.0	m^2 s^{-1}
Diapycnal Diffusivity	ϵ_V	5×10^{-5}	m^2 s^{-1}
Initial Surface Temperature	T_t	-1.9	^{o}C
Initial Bottom Temperature	T_b	1.0	^{o}C
Initial Surface Salinity	S_t	33.8	psu
Initial Bottom Salinity	S_b	34.7	psu
Maximum Ocean depth	H_ocean	720	m
Relaxation Time of Sponge Layer	T_sponge	0.1	days
Length of Sponge Layer	L_sponge	10	km
Ocean and iceberg model time step	dt	10	s
Elastic interactive force spring constant	κ_e	10^{-5}	s^{-2}

Table 1. Parameters used in the model. The ocean model parameters are as described in Asay-Davis et al [2016].
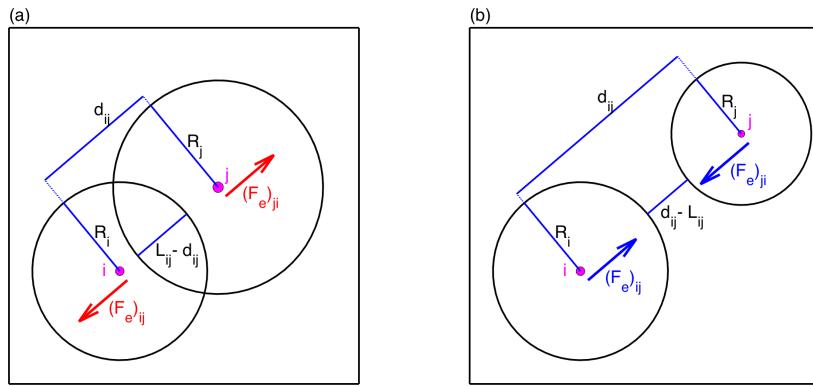
Figure 1. Schematic showing how tabular icebergs are constructed using Lagrangian elements. (a) Hierarchy of ice elements' physical structure: (i) Previous iceberg models represent icebergs using non-interacting point-particle elements; (ii) In the new framework ice elements are given finite extent so that they are able to interact with the ocean across multiple grid cells, and can interact with other elements; (iii) These finite extent elements can be joined together by numerical bonds (magenta lines) to form larger structures such as tabular icebergs. (b) Areal photograph of a tabular iceberg with elements superimposed over it to illustrate how the Lagrangian elements can be used to model tabular icebergs. In this schematic the ice elements (purple dots) are initialized in a staggered lattice covering the surface area of the iceberg. For purposes of mass aggregation, the ice elements are assumed to have hexagonal shape (red hexagons). For purposes of element interactions, the ice elements are assumed to be circular (black circles). Elements are initially bonded to adjacent elements using numerical bonds (magenta lines). These numerical bonds form equilateral triangles which give the shape rigidity. An ocean grid has been included (dashed cyan lines). The background photo is an areal photograph of iceberg PIIB (Area= 42 km^2) taken in Baffin Bay in 2012. A red ship can be identified on the bottom of the photo for scale.
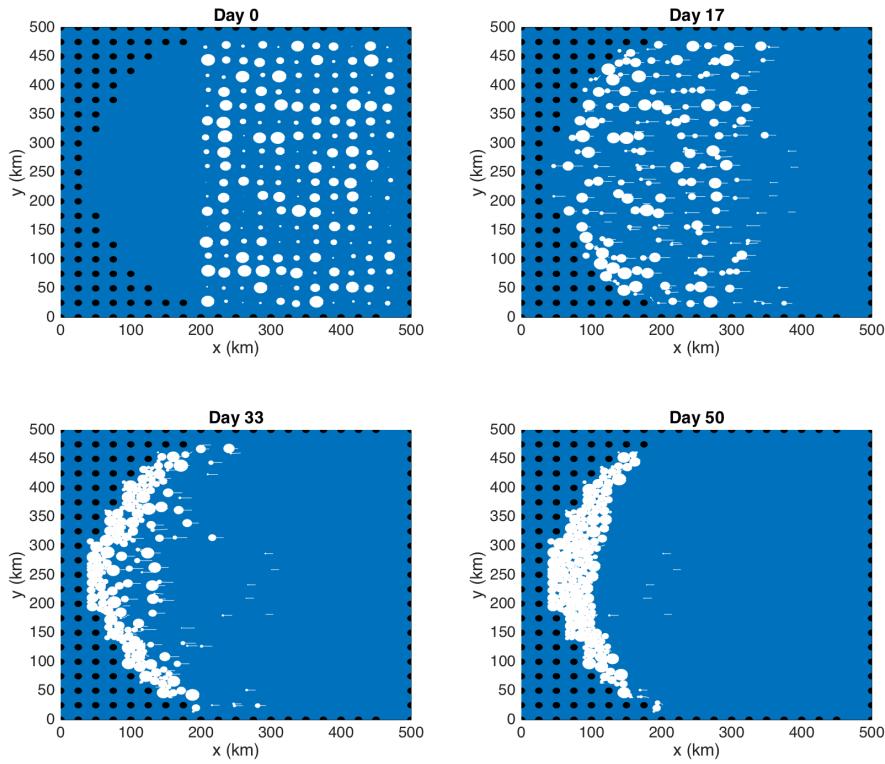
Figure 2. Snapshots of the sea surface temperature in the tabular iceberg calving simulation. Snapshots are taken (a) 7, (b) 15, and (c) 50 days after calving. Grid cells with ice mass > 10^4 kg are plotted in white, with grey shading indicating thinner ice. The dashed line in panel (c) shows the location of the vertical transects shown in Figures 8 and 11.
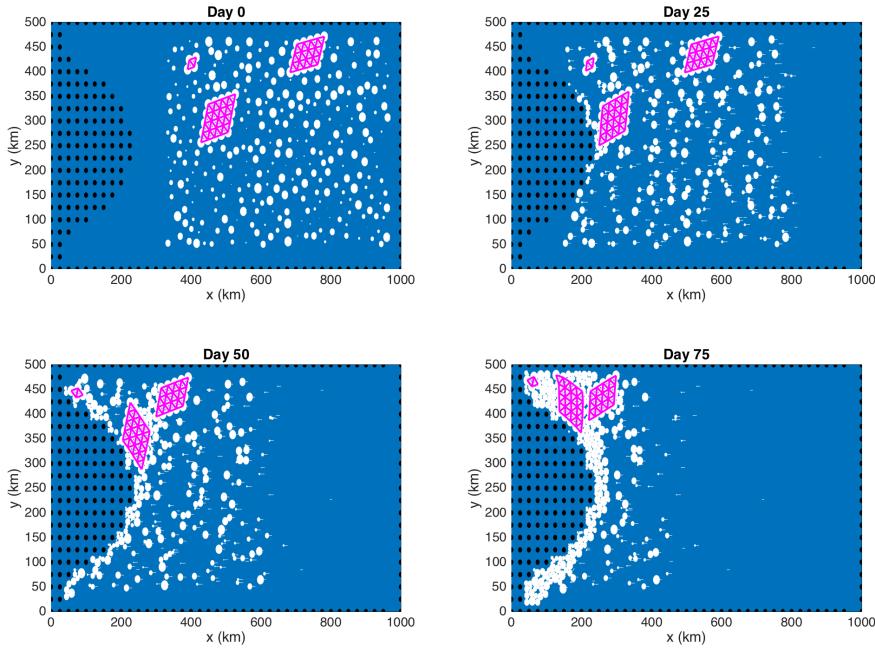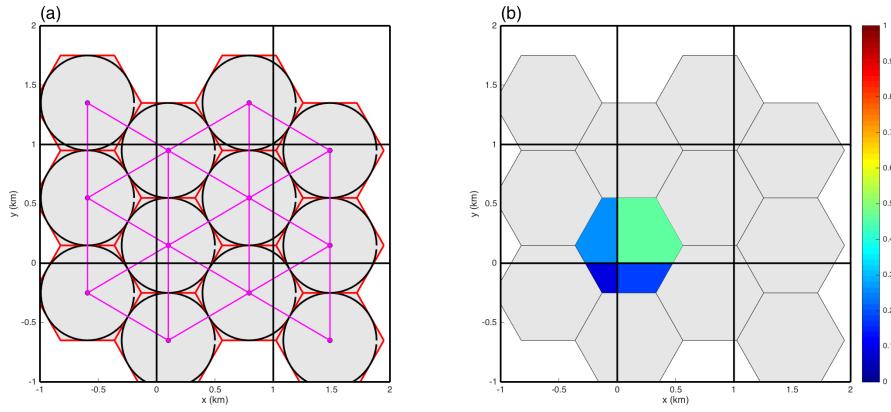
Figure 3. Diagram showing the (a) repulsive and (b) attractive elastic interactive forces between two elements, i and j. R_i and R_j are the interactive radii of element i and j, respectively. The distance between the centers of elements is denoted as d_{ij}. $L_{ij} = R_i + R_j$ is the critical-interactive-length scale. $(F_e)_{ij}$ and $(F_e)_{ji}$ are the elastic forces applied to elements i and j, respectively (equation 7). A frictional damping force is also applied, which opposes the relative velocity of the elements (not shown). The attractive forces are only applied when the two elements are bonded together (i.e.: $B_{ij} = 1$).
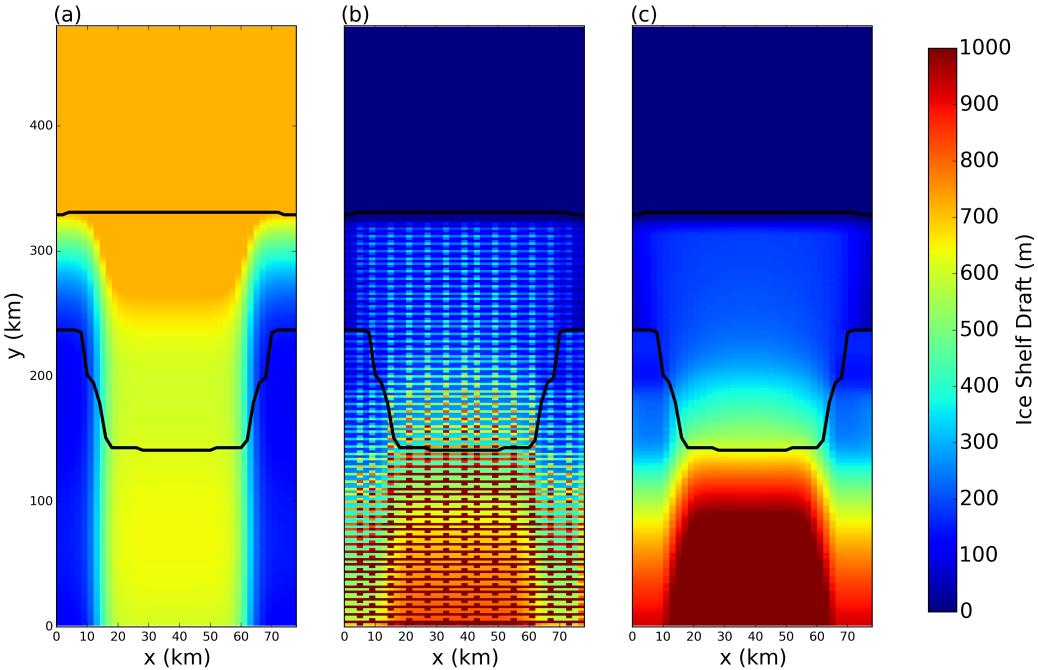
Figure 4. Results of an uncoupled (ice-only) simulation with no bonds between ice elements. Ice elements are initialized throughout the domain, as shown in the top left panel. The elements are forced by an imposed westward ocean current of u=0.1m/s (no ocean model is used). Forces due to sea surface slope, atmospheric drag, Coriolis and sea-ice drag are set to zero. The figure shows snapshots of ice element positions at time t=0, 17, 33 and 50 days. The size of the dots shows the surface area (and interaction radius) of each ice element. The white tails behind the elements show the elements' positions over the preceding two days. Land points are shown by black circles.
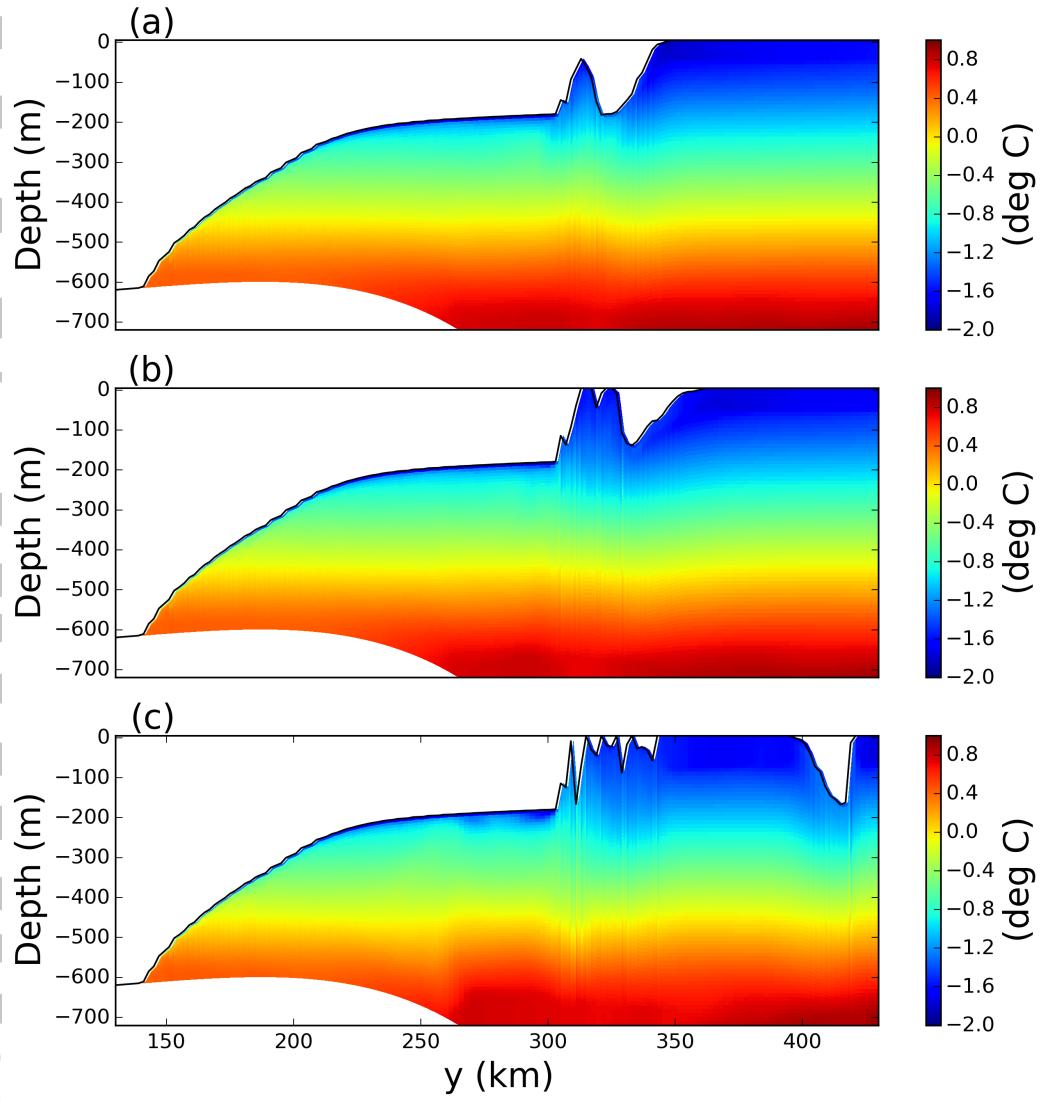
Figure 5. Results of an uncoupled (ice-only) simulation using bonds between elements. Ice elements are initialized throughout the domain, as shown in the top left panel. Three tabular icebergs are included, with 25, 16 and 4 elements respectively. The elements are forced by an imposed westward ocean current of u=0.1m/s (no ocean model is used). Forces due to sea surface slope, atmospheric drag, Coriolis and sea-ice drag are set to zero. The figure shows snapshots of ice element positions at time t=0, 25, 52, and 75 days. The size of the dots shows the surface area (and interaction radius) of each ice element. The white tails behind the elements show the elements' positions over the preceding two days. Bonds between ice elements are plotted in magenta. Land points are shown by black circles.
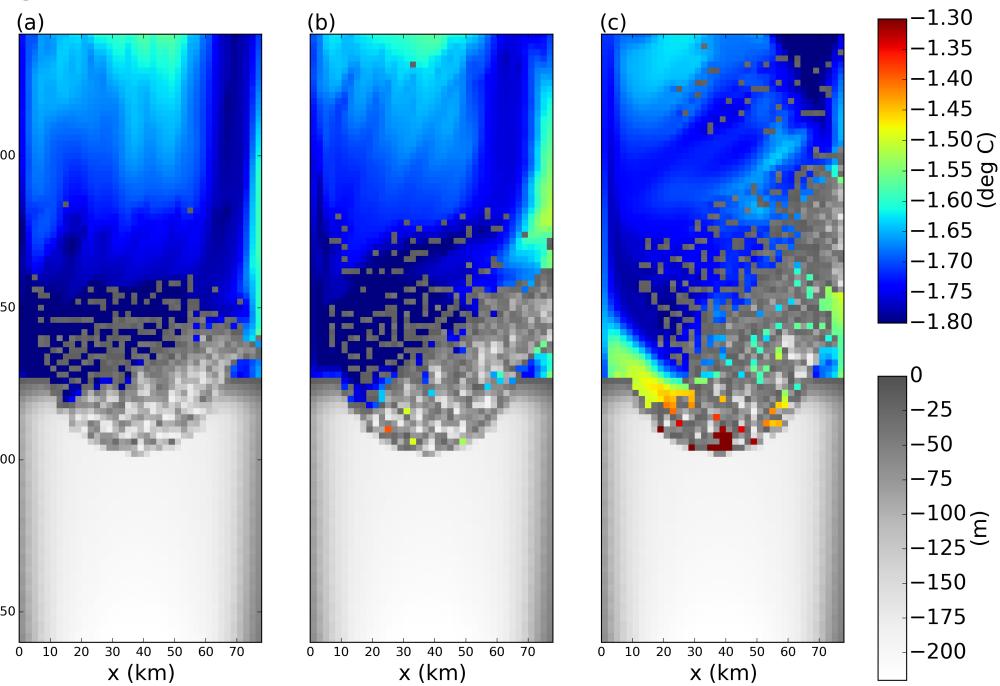
Figure 6. (a) Ice element packing and geometry: ice elements (purple dots) are initialized in a staggered lattice. For purposes of mass aggregation, the ice elements are assumed to have hexagonal shape (red hexagons). For purposes of element interactions, the ice elements are assumed to be circular (black circles). Elements are initially bonded to adjacent elements using numerical bonds (magenta lines). (b) Intersection of an hexagonal element and the ocean grid. The colors indicate the fraction of the hexagon that lies in each grid cell. These fractions are used as weights to spread the iceberg model properties to the ocean grid (see text for more details).
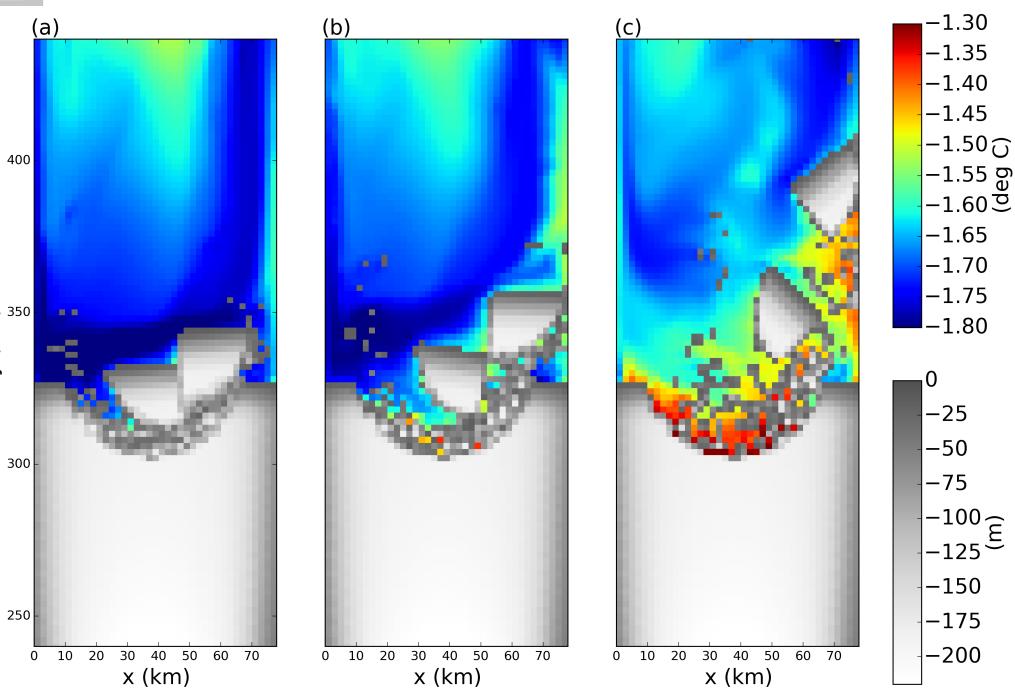
Figure 7. (a) Ocean bottom topography and (c) ice-shelf draft used to initialized the tabular iceberg calving simulation. The ice draft is calculated from the total mass in an ocean grid cell after the mass-spreading interpolation has been applied (as explained in Section 2.3). Panel (b) shows the initial ice draft that would be calculated if the mass-spreading interpolation were not used (i.e. elements treated as point masses). The lower and upper black lines denote the grounding line and ice shelf front, respectively.
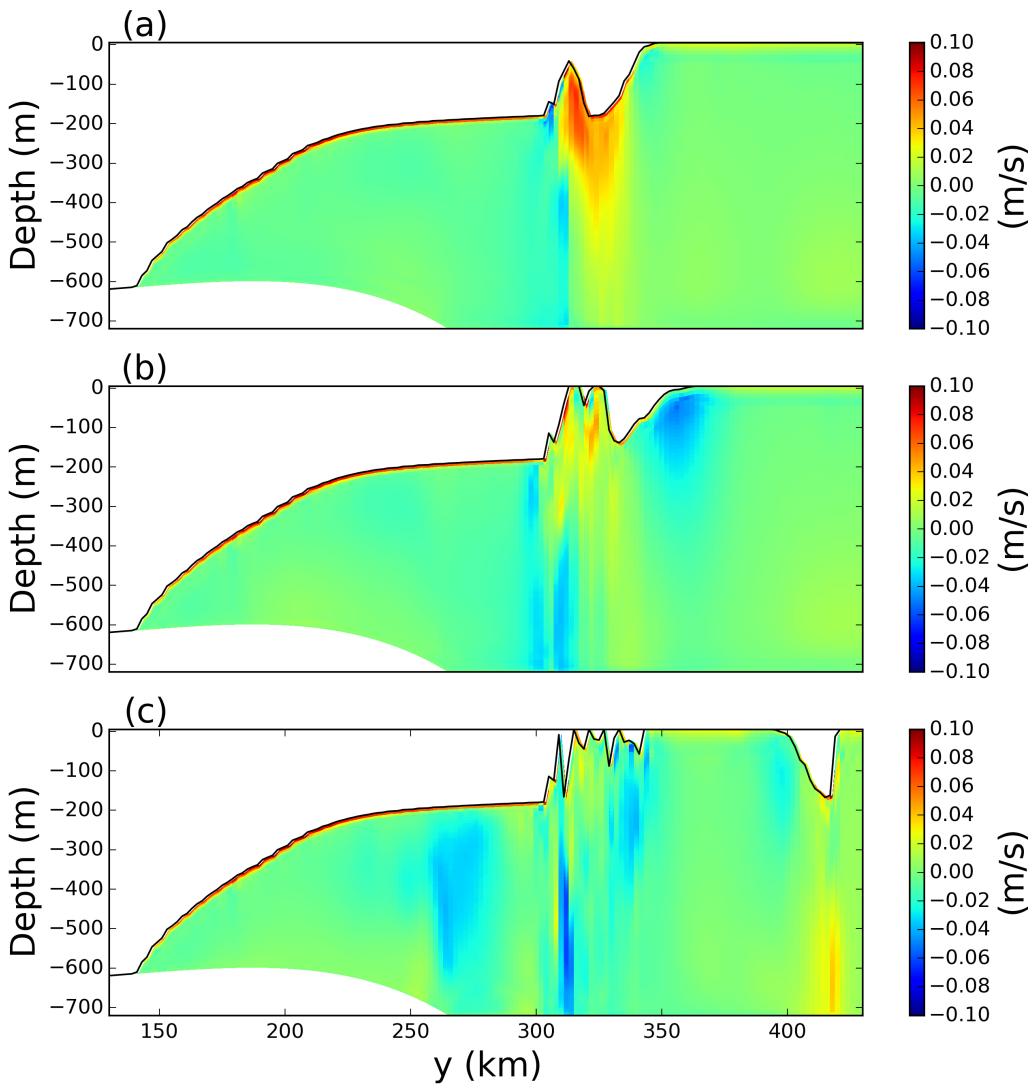
Figure 8. Snapshots of vertical sections of ocean temperature at x=54 km in the tabular-iceberg-calving Control experiment. Snapshots are taken (a) 7, (b) 15, and (c) 50 days after calving. The position of the vertical transects is shown by the dashed lines in Figure 2c.
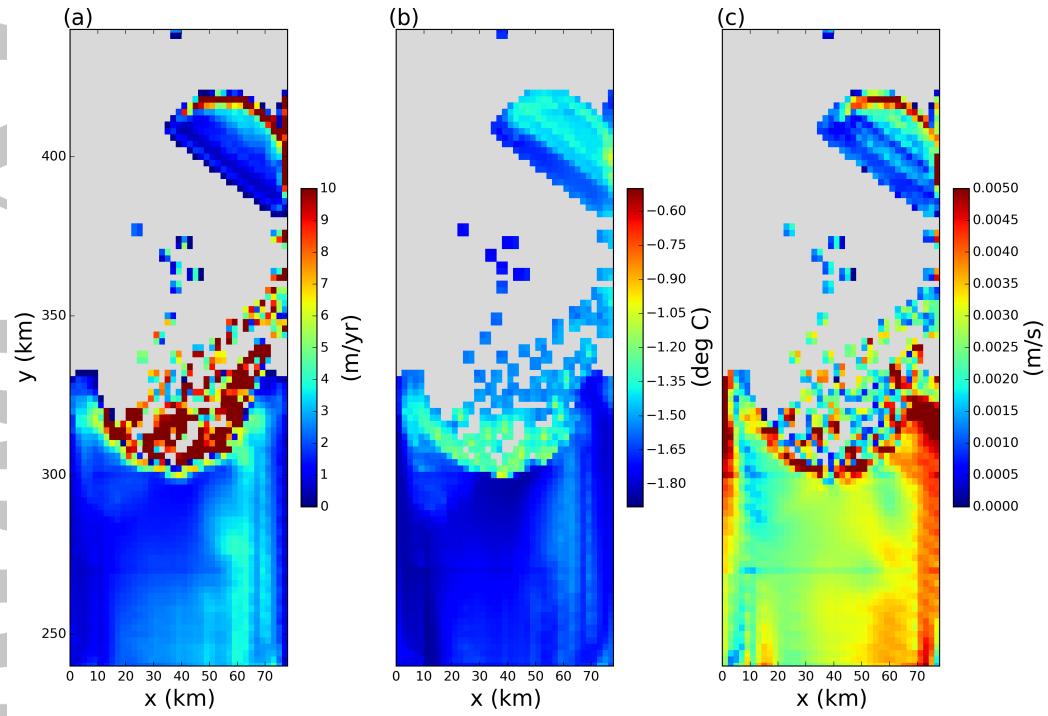
Figure 9. No bonds simulation: Snapshots of the sea surface temperature for a simulation where all bonds have been broken. Snapshots are taken (a) 7, (b) 15, and (c) 50 days after calving. Grid cells with ice mass $> 10^4$ kg are plotted in white, with grey shading indicating thinner ice.
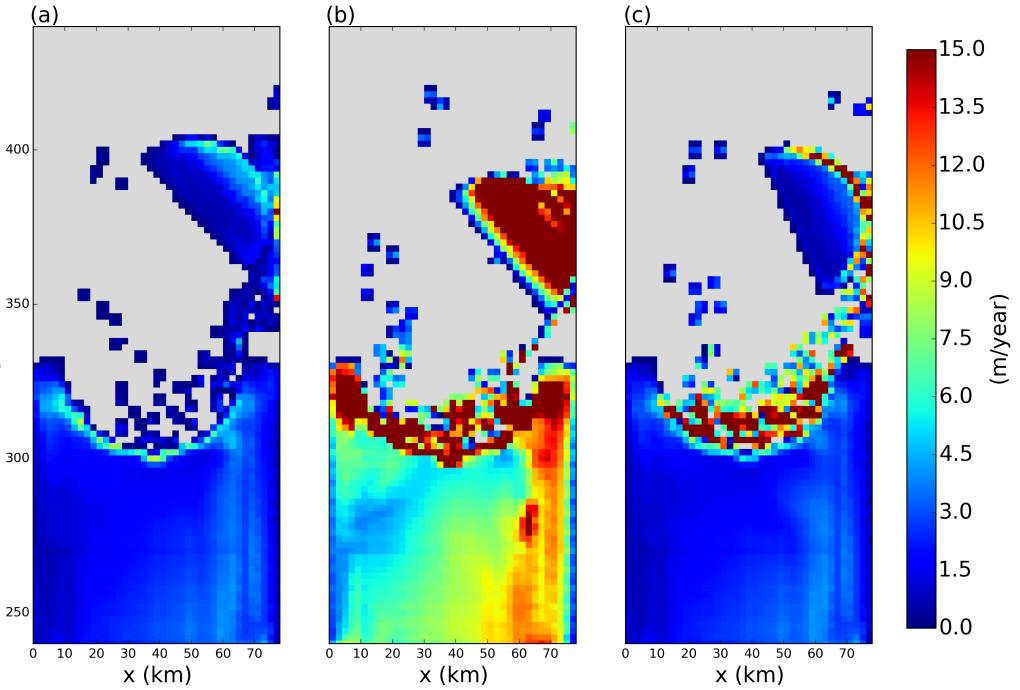
Figure 10. Iceberg splitting simulation: Snapshots of the sea surface temperature for the iceberg splitting simulation. Snapshots are taken (a) 7, (b) 15, and (c) 50 days after calving. Grid cells with ice mass $> 10^4$ kg are plotted in white, with grey shading indicating thinner ice.

Figure 11. Snapshots of vertical sections of meridional velocity at x=54 km in the tabular-iceberg-calving Control experiment. Snapshots are taken (a) 7, (b) 15, and (c) 50 days after calving. The position of the transects is shown by the dashed line in Figure 2c.

Figure 12. Results of the tabular-iceberg-calving experiment 50 days after the iceberg calves. The three panels show snapshots of the (a) melt rate, (b) top-of-ocean temperature and (c) the frictional velocity, u^*, at the base of the ice shelf. Ocean grid cells without ice are masked out in grey.

Figure 13. Results of three iceberg-calving experiments using different melt-rate parametrization. Panels show snapshots of the melt rate 30 days after calving for simulations using the (a) three-equation-model melt-rate parametrization [Holland and Jenkins, 1999], (b) point-particle-iceberg-melt parametrization [Gladstone et al, 2001], and (c) the mixed-melt-rate parametrization (introduced in Section 2.5.). Ocean grid cells without ice are masked out in grey.